The Astrophysical Journal, 809:89 (26pp), 2015 August 10 doi:10.1088/0004-637X/809/1/89

THE SPECTROSCOPIC PROPERTIES OF Lyα-EMITTERS AT $z \sim 2.7$: ESCAPING GAS AND PHOTONS FROM FAINT GALAXIES*

Ryan F. Trainor[1,4], Charles C. Steidel[2], Allison L. Strom[2], and Gwen C. Rudie[3,5]
[1] Department of Astronomy, University of California, Berkeley, 501 Campbell Hall, Berkeley, CA 94720, USA; trainor@berkeley.edu
[2] Cahill Center for Astrophysics, MC 249-17, 1200 E California Blvd, Pasadena, CA 91125, USA
[3] Carnegie Observatories, 813 Santa Barbara Street, Pasadena, CA 91101, USA
Received 2015 March 25; accepted 2015 July 6; published 2015 August 12

ABSTRACT

We present a spectroscopic survey of 318 faint ($\mathcal{R} \sim 27$, $L \sim 0.1L_*$), Lyα-emission-selected galaxies (LAEs) in regions centered on the positions of hyperluminous QSOs (HLQSOs) at $2.5 < z < 3$. A sample of 32 LAEs with rest-frame optical emission line spectra from *Keck*/Multi-Object Spectrometer For InfraRed Exploration (MOSFIRE) are used to interpret the LAE spectra in the context of their systemic redshifts. The fields are part of the Keck Baryonic Structure Survey, which includes substantial ancillary multi-wavelength imaging from both the ground and space. From a quantitative analysis of the diverse Lyα spectral morphologies, including line widths, asymmetries, and multi-peaked profiles, we find that peak widths and separations are typically smaller than among samples of more luminous continuum-selected galaxies (Lyman-break galaxies and their analogs; LBGs) at similar redshifts. We find tentative evidence for an association between Lyα spectral morphology and external illumination by the nearby HLQSO. Using the MOSFIRE subsample, we find that the peak of the resolved ($R \approx 1300$) Lyα line is shifted by $+200\,\mathrm{km\,s^{-1}}$ with respect to systemic across a diverse set of galaxies including both LAEs and LBGs. We also find a small number of objects with significantly blueshifted Lyα emission, a potential indicator of accreting gas. The Lyα-to-Hα line ratios measured for the MOSFIRE subset suggest that the LAEs in this sample have Lyα escape fractions $f_{\mathrm{esc,Ly}\alpha} \approx 30\%$, significantly higher than typical LBG samples. Using redshifts calibrated by our MOSFIRE sample, we construct composite LAE spectra, finding the first evidence for metal-enriched outflows in such intrinsically faint high-redshift galaxies. These outflows have smaller continuum covering fractions ($f_c \approx 0.3$) and velocities ($v_{\mathrm{ave}} \approx$ 100–200 $\mathrm{km\,s^{-1}}$, $v_{\mathrm{max}} \approx 500\,\mathrm{km\,s^{-1}}$) than those associated with typical LBGs, suggesting that the gas covering fraction is a likely driver of the high Lyα and Ly-continuum escape fractions of LAEs with respect to LBGs. Our results suggest a similar scaling of outflow velocity with star formation rate (SFR) as is observed at lower redshifts ($v_{\mathrm{outflow}} \sim \mathrm{SFR}^{0.25}$) and indicate that a substantial fraction of gas is ejected with $v > v_{\mathrm{esc}}$. Further observations, including deep spectroscopy in the observed near-IR, will further probe the evolution and enrichment of these galaxies in the context of their gaseous environments.

Key words: galaxies: formation – galaxies: high-redshift – intergalactic medium

1. INTRODUCTION

Stellar feedback plays a crucial role in galaxy formation. Massive stars enrich, heat, ionize, and expel gas throughout their lives and deaths, and understanding these processes is key to modeling the observational characteristics of galaxies at all redshifts. These characteristics include the low instantaneous efficiency of star formation (e.g., Kennicutt 1998), the low stellar masses and baryon content of galaxies (e.g., White & Frenk 1991; Kereš et al. 2009; Hopkins et al. 2014), and the presence and evolution of the mass–metallicity relationship of galaxies (e.g., Erb et al. 2006a; Andrews & Martini 2013; Steidel et al. 2014). Each of these observations requires that the majority of gas associated with galaxy halos is prohibited from forming stars, particularly in the lowest-mass galaxies. There are many potential causes for this inefficiency: the temperature, ionization, and/or kinematics of the gas may suppress its conversion into stars. Simulations can reproduce many characteristics of the stellar populations of galaxies simply by artificially delaying gas cooling or implementing other ad hoc solutions specific to these discrepancies; these naturally lack the predictive power of a feedback model based on the physics of star formation and supernovae themselves (see, e.g., Hummels et al. 2013; Hopkins et al. 2014).

In particular, many simulations struggle to reproduce properties of the circumgalactic medium (CGM; e.g., Rudie et al. 2012) of galaxies, which must be closely linked to the same feedback processes that shape their stellar populations. Studies of the gas in and around galaxy halos conclusively show that galaxies enrich their local CGM to large ($r \gtrsim r_{\mathrm{vir}}$) galactocentric radii (Aguirre et al. 2001; Adelberger et al. 2003, 2005; Pettini et al. 2003; Martin et al. 2010; Steidel et al. 2010; Turner et al. 2014), and it is expected that the chemistry and kinematics of these halos are tied to the properties of the enriched gaseous outflows seen ubiqitously in the spectra of high-redshift star-forming galaxies (Steidel et al. 1996; Pettini et al. 2001; Shapley et al. 2003; Jones et al. 2012; Martin et al. 2012).

Among Lyman-break galaxies and their analogs (hereafter referred to as LBGs), these outflows produce spectral signatures in both absorption and emission, allowing the characterization of the chemistry and kinematics of the outflows for gravitationally lensed sources (Pettini et al. 2000, 2002), or stacks of galaxies (Shapley et al. 2003; Steidel et al. 2010). Lyα emitters (LAEs) as a population are

* Based on data obtained at the W.M. Keck Observatory, which is operated as a scientific partnership among the California Institute of Technology, the University of California, and NASA, and was made possible by the generous financial support of the W.M. Keck Foundation.
[4] Miller Fellow.
[5] Carnegie-Princeton Fellow.

found to be younger, fainter, and less reddened (e.g., Gawiser et al. 2006) than LBGs on average,[6] so LAE surveys provide a complementary sample to LBGs for characterizing the effects of these gas flows (and stellar feedback in general) on galaxies over a broad range of ages and masses. Compared to most LBGs, LAEs may also "leak" a relatively large fraction of the Lyman-continuum (LyC) photons produced in their embedded star-forming regions (Mostardi et al. 2013; Nestor et al. 2013), which may be linked to the observed association between higher Lyα equivalent widths and lower neutral gas covering fractions among LBGs (Shapley et al. 2003; Jones et al. 2013). Therefore, LAEs may be most analogous to those galaxies that dominate the reionization of the universe (e.g., Robertson et al. 2013; Dressler et al. 2015).

Most Lyα-selected galaxies are too faint for continuum absorption features to be easily observed. At low redshifts, the Lyα Reference Sample (LARS; Hayes et al. 2013; Östlin et al. 2014) includes 14 local galaxies with *Hubble Space Telescope* (*HST*) imaging and spectroscopy of their Lyα emission. Rivera-Thorsen et al. (2015) analyze metal absorption and Lyα emission from these galaxies, finding that gaseous outflows and the covering fractions of absorbers play a strong role in modulating Lyα escape (see also similar results by Wofford et al. 2013). The few measurements of interstellar absorption in high-redshift LAE spectra come from especially bright examples (Hashimoto et al. 2013; Shibuya et al. 2014), with continuum magnitudes ($B \sim 24$, $L \sim L_*$) bright enough to fall into typical samples of LBGs.[7] However, it is the faint LAEs that provide the most interesting environment for studying the kinematics of gas and galaxies. Assuming that the feedback processes ubiquitous in LBGs extend to the earliest and faintest galaxies, then the effect of even faint galaxies on their surrounding gaseous environments must be taken into account when modeling the enrichment of the circumgalactic and intergalactic media (CGM and IGM; e.g., Steidel et al. 2010) and its transparency to ionizing photons (e.g., Rudie et al. 2013; Schenker et al. 2013). Furthermore, the low masses and star formation rates (SFR) of galaxies selected as LAEs may enable the detection of the gas infall predicted by simulations (Birnboim & Dekel 2003; Kereš et al. 2005; and others) whereas in LBGs with stronger SFRs, gaseous outflows may dominate over infall in determining the state of circumgalactic gas.

Regions of the sky around bright QSOs provide particularly advantageous environments for LAE surveys. Hyperluminous QSOs inhabit known galaxy overdensities (Trainor & Steidel 2012) and thereby yield a large number of LAEs within a single telescope pointing and narrowband-selected redshift interval. Additionally, the ionizing fields of the QSOs can boost the Lyα emission of faint, gas-rich galaxies through Lyα "fluorescence" (Hogan & Weymann 1987; Adelberger et al. 2006; Cantalupo et al. 2007, 2012; Kollmeier et al. 2010; Trainor & Steidel 2013). These effects make QSO fields extremely efficient for the selection and follow-up of faint LAEs. Fluorescent Lyα emission can allow the characterization of the QSO radiative geometry and history (Trainor & Steidel 2013), but it also provides a means of selecting galaxies irrespective of their intrinsic stellar luminosities. LAEs selected in these regions may include "dark galaxies" (Cantalupo et al. 2012), halos of gas and dark matter in which only negligible star formation has occurred. Whether or not such "dark" objects are observable, the fluorescent boost of nearby QSOs may allow us to probe an even greater range of galaxy properties than typical LAE surveys alone.

In this paper, we present rest-frame UV spectroscopy from a large (68,000 cMpc^3) narrowband survey conducted in eight QSO fields with $2.55 < z_{\rm QSO} < 2.85$. All eight fields are part of the Keck Baryonic Structure Survey (KBSS; Rudie et al. 2012), and this Lyα survey (designated KBSS-Lyα) is complementary to the original KBSS for probing the interactions of QSOs, galaxies, and gas at the peak redshifts of star formation. The authors note that the effect of the bright QSOs in the KBSS-Lyα fields on their nearby galaxies is not generally known, but the QSO-induced contribution to the Lyα emission is expected to be independent of the intrinsic star formation properties of these galaxies. In this paper, we generally assume that the kinematic and transmissive properties of the KBSS-Lyα LAEs are most directly related to their internal star formation and stellar populations. However, the results of our analysis that may depend strongly on QSO illumination and proximity are noted explicitly. Future work will consider the effect of the QSO on associated galaxies in greater detail.

The spectroscopic component of the KBSS-Lyα survey is described in Section 2. In Section 3, we present the properties of the Lyα emission lines, including analysis of the Lyα escape fraction, spectral morphology, and kinematics in relation to comparison samples of continuum-bright galaxies. In Section 4, we present measurements of metal absorption lines in the stacked continuum spectra of the rest-UV spectroscopic sample and characterize the ionization, covering fraction, and kinematics of star formation driven outflows in the LAEs. A brief discussion of these results in the context of the physical properties of the galaxies and previous work is given in Section 5, and our results are summarized in Section 6. Physical quantities are given in observable units when possible, but a ΛCDM universe with $(\Omega_{\rm m},\ \Omega_\Lambda,\ H_0) = (0.3,\ 0.7,\ 70\,{\rm km\,s^{-1}})$ is assumed when necessary.

2. OBSERVATIONS

2.1. LAE Sample

The full parent sample of ~800 photometrically identified LAEs will be described separately (R. Trainor et al. 2015, in preparation); this LAE sample was also used and discussed by Trainor & Steidel (2013). LAEs were identified on the basis of paired narrowband and broadband observations (from Keck I/LRIS-B) using a custom set of narrowband filters. A total of four narrowband filters were used, each with a bandpass constructed to select the wavelength of Lyα at one or more QSO redshifts (Figure 1). Objects were identified and photometry was performed using SExtractor in one- and two-image modes to extract narrowband and broadband magnitudes ($m_{\rm NB}$ and $m_{\rm BB}$) sampling Lyα. Hereafter, $m_{\rm BB}$ refers to the measured LAE magnitude in the B and/or G filter used to estimate the continuum emission near Lyα, whichever is better matched at a given redshift (Table 1). Because the B/G filter bandpasses include the Lyα emission line, we use $\mathcal{R}$-band

[6] Note, however, that all LBGs emit at least low-level Lyα emission, and all LAEs would display Lyman breaks in sufficiently sensitive broadband images or spectra (Steidel et al. 2011).

[7] For example, 25% of the 811 "LBGs" in Shapley et al. (2003) have $W_{{\rm Ly}\alpha} > 20$ Å and spectroscopic properties similar to these bright-LAE samples.

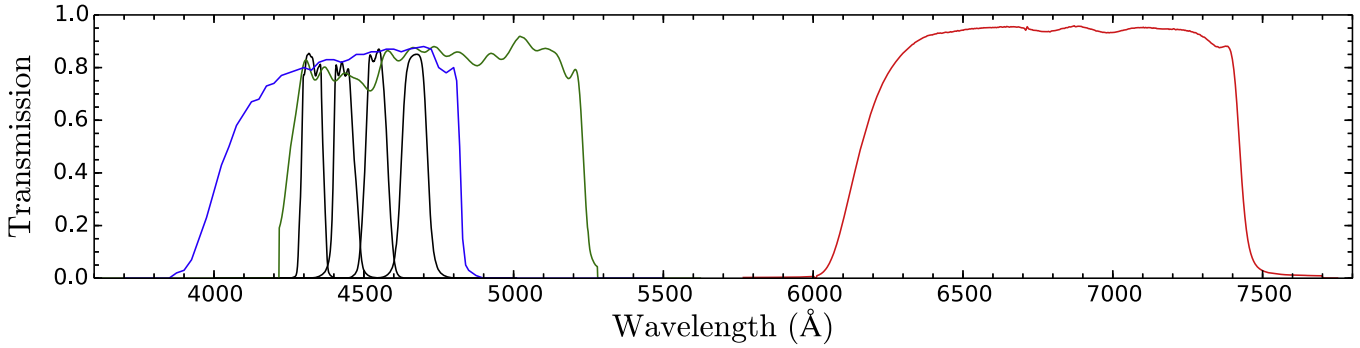

Figure 1. Bandpasses of the primary narrowband and broadband filters used to select and characterize the LAEs in this paper. Black curves are the four narrowband filters (from left to right: NB4325, NB4430, NB4535, NB4670, with names reflecting the central wavelength in Angstroms). The blue, green, and red curves show the bandpasses of the LRIS B, G, and $\mathcal{R}$ filters, respectively.

Table 1
Lyα-emitter Field Descriptions

QSO Field	z_Q (±0.001)	NB Filter	BB Filter	N_{spec}
Q0100+13 (PHL957)	2.721	NB4535	B+G	20
HS0105+1619	2.652	NB4430	B	22
Q0142−10 (UM673a)	2.743	NB4535	B+G	22
Q1009+29 (CSO 38)	2.652	NB4430	B	35
HS1442+2931	2.660	NB4430	B	41
HS1549+1919	2.843	NB4670	G	95
HS1700+6416	2.751	NB4535	B+G	20
Q2343+12	2.573	NB4325	B	63

measurements to sample the continuum without Lyα contamination. We conducted follow-up spectroscopy of the subset of objects identified to have a narrowband color excess $m_{BB} - m_{NB} > 0.6$, which corresponds to a limit in rest-frame Lyα equivalent width $W_{Ly\alpha} \gtrsim 20$ Å. The success of our spectroscopic follow-up observations dropped significantly for $m_{NB} > 26.5$, so this limit (approximately the 3σ depth of our narrowband observations) was adopted as the faint cut-off for the photometric and spectroscopic samples. This magnitude limit corresponds to an integrated narrowband flux $F_{Ly\alpha} \approx 1 \times 10^{-17}$ erg s^{-1} cm^{-2} for a continuum-free Lyα emission line, or $F_{Ly\alpha} \approx 6 \times 10^{-18}$ erg s^{-1} cm^{-2} for an emission line with our median value of $\langle W_{Ly\alpha} \rangle \approx 40$ Å. The apparent magnitude distribution of both the parent sample and the spectroscopic subsample of LAEs discussed in this paper are given in Figure 2. Both the spectroscopic and photometric samples have median $\langle \mathcal{R}_{AB}(6930\text{ Å}) \rangle \approx 27$. According to the galaxy luminosity functions measured by Reddy et al. (2008), this continuum magnitude corresponds to $L \sim 0.1 L_*$ at $z \sim 2.7$. Details of the QSO fields and the spectroscopic sample are given in Table 1.

2.2. UV Spectroscopic Observations

Rest-UV spectra were obtained with Keck I/LRIS-B in the multislit mode using the 600/4000 grism and 560 nm dichroic. All objects were observed with 1″.2 wide slits, but the spectral resolution is limited by the 0″.6–0″.8 seeing disk for these (typically spatially unresolved) LAEs. The effective resolution near the observed Lyα wavelength for these spectra is $R \sim 1300$, corresponding to a velocity resolution $\sigma_v \sim 100$ km s^{-1}. Spectroscopic observations were performed in sets of 3–4 1800 s exposures, for a total of 1.5–2 hr of total

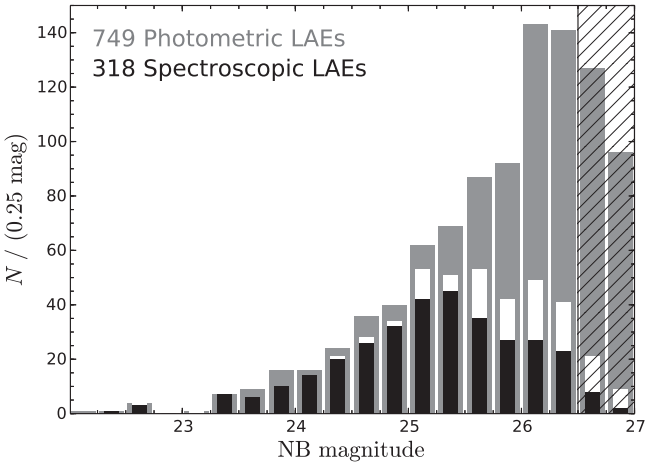

Figure 2. Apparent magnitude distribution of all photometric (gray) and spectroscopic (black) LAEs observed in the survey. NB magnitude denotes the apparent magnitude of each LAE in the narrowband (NB) filter used to select it. The white sections of the bars denote the number of LAEs in each bin observed spectroscopically for which no line was detected by our algorithm. These objects are excluded from the spectroscopic sample of LAEs. For $m_{NB} > 26.5$ (hatched region), the success rate of spectroscopic identification of the Lyα emission line dropped precipitously; for this reason, this paper primarily considers only those LAEs with a NB magnitude brighter than 26.5 ($F_{Ly\alpha} \geqslant 6 - 10 \times 10^{-18}$ erg s^{-1} cm^{-2}).

integration time per object. By the completion of the survey, we had obtained spectra for 415 of the 749 photometric LAE candidates, with some candidates observed on as many as three different masks. The observations were conducted and reduced in essentially the same manner as those of the KBSS and preceding surveys, a detailed description of which can be found in Steidel et al. (2003, 2004). Specifically, masks were constructed and targets assigned as described by Steidel et al. (2003), but with a minimum slit length of 11″ in order to provide better background subtraction for continuum-faint ($\mathcal{R} \sim 27$) sources. The data were reduced (including flat-fielding, cosmic-ray rejection, background subtraction, flexure compensation, and wavelength/flux calibration) using a custom set of IRAF scripts as described in Steidel et al. (2003). The two-dimensional spectra were rectified using flat-field observations, and one-dimensional spectra were then extracted using the IRAF task *apall* with 10 pixel apertures (1″.35, ∼2× the seeing FWHM). We detect little or no continuum emission in individual spectra, so all pixels in the aperture received equal weighting during the extraction and the object trace was not allowed to vary with wavelength along the

rectified 2D spectrum. Note that the Keck I Cassegrain Atmospheric Dispersion Corrector removes the wavelength-dependent shifts in object position due to differential atmospheric refraction. The two-dimensional spectra were binned in two-pixel blocks along the wavelength axis during readout, and the one-dimensional extracted spectra were resampled to the median resulting wavelength scale of the observations, 1.26 Å pix^{-1}.

The resulting one-dimensional spectra were then subjected to an automated line-detection algorithm described here. First, each spectrum was smoothed with a kernel corresponding to the instrumental resolution (∼3.5 Å FWHM). A detection region of the spectrum was then isolated: in order to ensure that spectroscopically detected objects corresponded to their NB-selected counterparts, the algorithm only located emission lines that would fall between the 10% power points of the corresponding NB filter used to select them. The highest peak in this detection region was then used to define the first guess at the emission line wavelength. The significance of the detected peak was then estimated by

$$P(y) = 1 - \left(\int_{y_{\rm max}/\sigma_y}^{\infty} G(x)\, dx \right)^{n_{\rm pix}}, \quad (1)$$

where $y_{\rm max}$ is the observed peak value (minus any measured continuum) in the smoothed spectrum, σ_y is the sample standard deviation of the smoothed spectrum in the detection region, $G(x) = e^{-x^2/2}/\sqrt{2\pi}$ is the normal distribution function, and $n_{\rm pix}$ is the number of pixels in the detection region of the spectrum. In this way, $P(y)$ represents the probability of measuring one or more pixels with value $y \geqslant y_{\rm max}$ within the detection region under the null hypothesis that the pixel values are normally distributed with variance σ_y^2. Spectra with $P(y) \geqslant 0.05$ were rejected as non-detections, while those with $P(y) < 0.05$ were designated candidate emission lines. This threshold was chosen because it closely reproduces the samples of significant and non-significant spectral Lyα detections identified by eye. The median signal-to-noise ratio (S/N) of the spectroscopic detections is 10.1. The total flux in each candidate emission line was then estimated both by Gaussian fitting and by direct integration of the unsmoothed spectrum. Finally, the line was re-fit using an asymmetric line profile:

$$f_\lambda(\lambda) = \begin{cases} Ae^{-(\lambda-\mu)/2\sigma_{\rm blue}^2} & \lambda < \mu \\ Ae^{-(\lambda-\mu)/2\sigma_{\rm red}^2} & \lambda \geqslant \mu \end{cases} \quad (2)$$

$$\alpha_{\rm asym} \equiv \sigma_{\rm red}/\sigma_{\rm blue}. \quad (3)$$

Here, $\sigma_{\rm blue}$ represents the line-width measured from the "blue" side of the peak ($\lambda < \mu$), while $\sigma_{\rm red}$ is the width on the "red" side of the peak ($\lambda > \mu$), where μ is the fitted peak of the Lyα profile. From these quantities, we define the asymmetry of the line shape, $\alpha_{\rm asym}$, a potential diagnostic of Lyα escape physics (Chonis et al. 2013; Zheng & Wallace 2014). Many lines were found to be multi-peaked, defined by the existence of a second peak in the smoothed spectrum at least 2.5σ above the continuum and within 1500 km s^{-1} of the primary peak, separated from the primary peak by an inter-peak minimum. As these secondary peaks typically have lower S/N than the primary peak, they were fit using symmetric Gaussian profiles. No more than two Gaussian peaks were allowed in each fit. When fitting line profiles, the fits were constrained such that the fit width σ (both $\sigma_{\rm blue}$ and $\sigma_{\rm red}$ for asymmetric profiles) could not fall below the instrument resolution ($\sigma > 1.5$ Å). Measured line widths, asymmetries, and multi-peaked profiles are discussed in detail in Section 3.3. As demonstrated in that section, the resolution of these spectra is sufficient to resolve the peak width, separation, and asymmetry for the typical objects in our survey. However, we note that these spectra may not resolve spectral features on very small ($\delta v \lesssim 100$ km s^{-1}) velocity scales, such as those predicted by radiative transfer models and observed in some high-resolution spectra of bright or nearby galaxies (Verhamme et al. 2008; Martin et al. 2015).

The observed wavelength of the Lyα emission line was measured via two methods: direct integration of the unsmoothed spectrum (i.e., the flux-weighted line centroid), and the fit value of μ (i.e., the peak of the fit asymmetric Gaussian profile). For multi-peaked lines, the primary peak is that which was detected by our first-pass line detection algorithm (i.e., the most significant spike in the smoothed spectrum). Henceforth in this paper, $z_{{\rm Ly}\alpha,{\rm peak}}$ denotes the redshift of the Lyα line derived from the asymmetric Gaussian peak, while $z_{{\rm Ly}\alpha,{\rm ave}}$ refers to the redshift derived from direct integration; these values are compared in Section 3.2.

We used spectroscopic and photometric cuts to eliminate non-Lyα contaminants from our sample. Because the narrowband filters used in this survey all have central wavelengths $\lambda_c < 4900$ Å, [O III] emitters are excluded by design. [O II] emitters ($\lambda\lambda$3726,3729) may be selected at $z \sim 0.15$–0.25 depending on the specific narrowband filter used for each field. However, the total comoving volume selected by these filters is ∼50× larger for Lyα at $z \sim 2.6$ than for [O II] at $z \sim 0.2$. The [O II] luminosity density is also very low at $z \approx 0.2$ with respect to higher redshifts, and objects with [O II] equivalent widths in emission greater than our observed-frame cut off ($W_{\rm obs} > 72$ Å) are extremely rare (Hogg et al. 1998; Ciardullo et al. 2013). Furthermore, the [O II] doublet should be marginally resolved in our $\sigma_v \approx 100$ km s^{-1} spectra, with a line separation $\Delta\lambda_{\rm OII} \approx 220$ km s^{-1}. As shown in Section 3.3, there is no detected population of objects that have multi-peaked emission lines with $\Delta v_{\rm peaks} \approx 200$ km s^{-1}, so we do not expect that low-redshift [O II] emitters are a significant source of contamination to our photometric or spectroscopic samples.

The observed spectral range for each spectrum depends on the location of the corresponding slit on the mask, but most slits were placed to cover a rest-wavelength range 900 Å $\lesssim \lambda \lesssim$ 1500 Å at $z \sim 2.7$. As such, other contaminants to the LAE sample were considered by searching for anomalous emission lines outside of the Lyα detection window. A small number of such objects were found. All the spectroscopically identified contaminants were lower-redshift active galactic nuclei (AGNs) in which strong C IV λ1550 ($z \sim 1.9$) or He II λ1640 ($z \sim 1.7$) emission was detected by our narrowband filter. In each case, Lyα, C IV, and He II emission are all present with high equivalent width. Five objects were found where the narrowband excess was caused by C IV emission, and another 5 objects were selected due to He II emission falling in the narrowband passband. All 10 objects were removed from both the spectroscopic and photometric samples. These constraints define a sample of 422 spectra for 318 unique LAEs. Using the contamination results, we estimate the contamination fraction for the photometric sample to be $10/(318+10) = 3.0\%$.

To facilitate comparison with samples of continuum-bright galaxies, we also analyze a sample of 65 LBGs from the KBSS-MOSFIRE (Steidel et al. 2014). These 65 galaxies are hereafter described as the KBSS LBG sample. Details of the object selection and data collection and reduction are described by Steidel et al. (2014) and references therein. The 65 KBSS LBG galaxies discussed here are a small subsample of the entire KBSS-MOSFIRE catalog that meet the following requirements:

1. rest-UV spectra acquired using the same LRIS instrument setup (including the 600-line grism) as the KBSS-Lyα LAEs;
2. Lyα emission spectroscopically detected by the same line-detection algorithm employed for the KBSS-Lyα LAEs (56% of the above objects);
3. systemic redshift measurements acquired as part of the KBSS-MOSFIRE via rest-frame optical emission lines (similar to the KBSS-Lyα Multi-Object Spectrometer For InfraRed Exploration (MOSFIRE) subsample described in Section 2.3);
4. a lack of broad, high-equivalent width C IV emission indicative of AGN activity (97% of objects meet this requirement).

The KBSS LBG sample provides a means of comparing the spectral properties of LAEs to objects $\sim$10$\times$ brighter in the UV continuum using the same spectral resolution and analysis methods. Note that $\sim$50% of all galaxies in the full KBSS-MOSFIRE sample have UV redshifts measurable only in continuum absorption lines. Such objects cannot be selected by narrowband searches, so they were omitted from the KBSS LBG sample to ensure appropriate comparison (criterion #2 above). However, note also that the KBSS LAEs have no photometric cut based on $W_{\rm Ly\alpha}$, as these galaxies occupy a large range of redshifts and do not generally have narrowband images probing their Lyα emission.

The line-fitting algorithm was changed slightly for the KBSS LBG spectra to accommodate the strong continuum, which often varies significantly on the redward and blueward sides of the Lyα line. When fitting the LBGs, a free parameter was added to provide a linear fit to the continuum over the line region, but the one-peak or two-peak asymmetric Gaussian fits were otherwise conducted in an identical manner for the LAE and LBG samples. In Section 4.3, we also consider a composite LBG spectrum from a survey of LBGs at $z\sim3$ (C. Steidel et al. 2015, in preparation). The data collection and reduction of the objects in this composite spectrum are similar to the other LAEs and LBGs described above and will be discussed in detail in future work.

QSO redshifts were determined as described in Trainor & Steidel (2012) and have estimated uncertainties $\sigma_{z,\rm QSO}\approx 270\,{\rm km\,s^{-1}}$. The redshift distribution of LAEs with respect to their nearby QSO is shown for each field in Figure 3. On small scales, the redshift distribution of LAEs with respect to the hyperluminous QSOs (HLQSOs) is more meaningful to consider as a distribution of velocities. The relative LAE-QSO velocities are calculated as $v_{\rm LAE}=c(z_{\rm LAE}-z_{\rm QSO})/(1+z_{\rm QSO})$. The distribution of QSO-centric velocities for our entire spectroscopic LAE sample is given in Figure 4. Here and elsewhere in this paper we assume that the LAEs have systemic redshifts given by $z_{\rm LAE}=z_{\rm Ly\alpha}-200\,{\rm km\,s^{-1}}$ to account for the typical redshift of the Lyα emission peak with respect to systemic derived from our MOSFIRE data set (Section 2.3).

2.3. MOSFIRE Spectroscopic Sample

For a small subset of these Lyα-selected objects, rest-frame optical spectra were also obtained via the new MOSFIRE (McLean et al. 2010, 2012) on the Keck I telescope. These data were taken over the course of the KBSS-MOSFIRE survey (Steidel et al. 2014). All the MOSFIRE data considered in this analysis are from the field around the HLQSO Q2343+12 ($z=2.573$). *H*-band and/or *K*-band spectra were obtained for 43 LAEs in this field and reduced via the MOSFIRE-DRP; the observational strategies employed and reduction software are described in Steidel et al. (2014). Redshift fitting and one-dimensional spectral extraction were performed using the IDL program MOSPEC (A. Strom et al. 2015, in preparation). With $0\farcs7$ slits, these spectra have $R\sim3600$, $\sigma_v\sim35\,{\rm km\,s^{-1}}$. Of the 43 observed LAEs, 32 yielded robust redshifts via measurement of Hα (*K*-band, 29 objects), Hβ, and/or the [O III] $\lambda\lambda$4959,5007 doublet (*H*-band, 12 objects) in emission. Nine objects have measured redshifts in both bands. Four of the MOSFIRE objects do not meet the Lyα equivalent width threshold employed here to define LAEs in a strict sense ($W_{\rm Ly\alpha}>20$ Å), but these four are kept in the sample because they were otherwise selected via the same photometric techniques used to define the rest of the sample, and they all display strong Lyα emission in their spectra. Furthermore, the other photometric and spectroscopic properties of these four objects are typical with respect to the remainder of the MOSFIRE sample.

Additional information on these spectra is given in Table 2 and Figure 5. The redshift measured from the MOSFIRE spectra, whether from the *H* or *K* band, is hereafter denoted by $z_{\rm neb}$. In the nine cases where a measurement was obtained in both bands, the redshift measurement from the higher-S/N *H* was used, but both bands generally agree quite closely: the median redshift difference for the two bands is $17\,{\rm km\,s^{-1}}$, roughly half the $\sigma\sim35\,{\rm km\,s^{-1}}$ resolution of these spectra. The fit redshifts have typical uncertainties $\sigma_H\sim5\,{\rm km\ s^{-1}}$ and $\sigma_K\sim7$–$20\,{\rm km\ s^{-1}}$ for the *H*- and *K*-band redshifts, respectively, based on their Gaussian fits.

Our pre-existing $\mathcal{R}$-band image in the Q2343 field is rotated with respect to the narrowband and *B*-band images used to select LAEs, so $\sim$16% of the Lyα-imaged field does not currently have $\mathcal{R}$-band coverage. Objects falling in this region are omitted when discussing average $\mathcal{R}$-band properties of the LAEs. In particular, 4 of the 32 MOSFIRE LAEs have no measured $\mathcal{R}$ magnitudes (Table 2), but their continuum properties in other bands (*B* and NIR where available) are consistent with those falling within our existing $\mathcal{R}$ coverage. The 3σ $\mathcal{R}$-band limit is reported in Table 2 for objects with measured $\mathcal{R}$ magnitudes fainter than that value.

Velocity dispersions are measured (or constrained) for each MOSFIRE LAE from the Gaussian fit to the detected spectral line. As above, the highest-S/N line (generally [O III] λ5007) width is used when multiple lines are detected. The measured line widths (deconvolved from the instrumental profile) range from $\sigma_{\rm neb}=14\pm9$ to $114\pm8\,{\rm km\,s^{-1}}$ (Table 2), with a median $\langle\sigma_{\rm neb}\rangle=34\,{\rm km\,s^{-1}}$. The object with the largest fit dispersion (Q2343-NB2807) has a two-peaked nebular line profile that is not well-fit by a single Gaussian; with the exception of this object, no LAE has a fit dispersion larger than $73\,{\rm km\ s^{-1}}$. Ten objects have line widths consistent with the MOSFIRE instrument profile and are given as limits ($\sigma_{\rm neb}<35\,{\rm km\,s^{-1}}$). The LAEs are generally unresolved in our ground-based images, and further analysis of the limited *HST*/WFC3

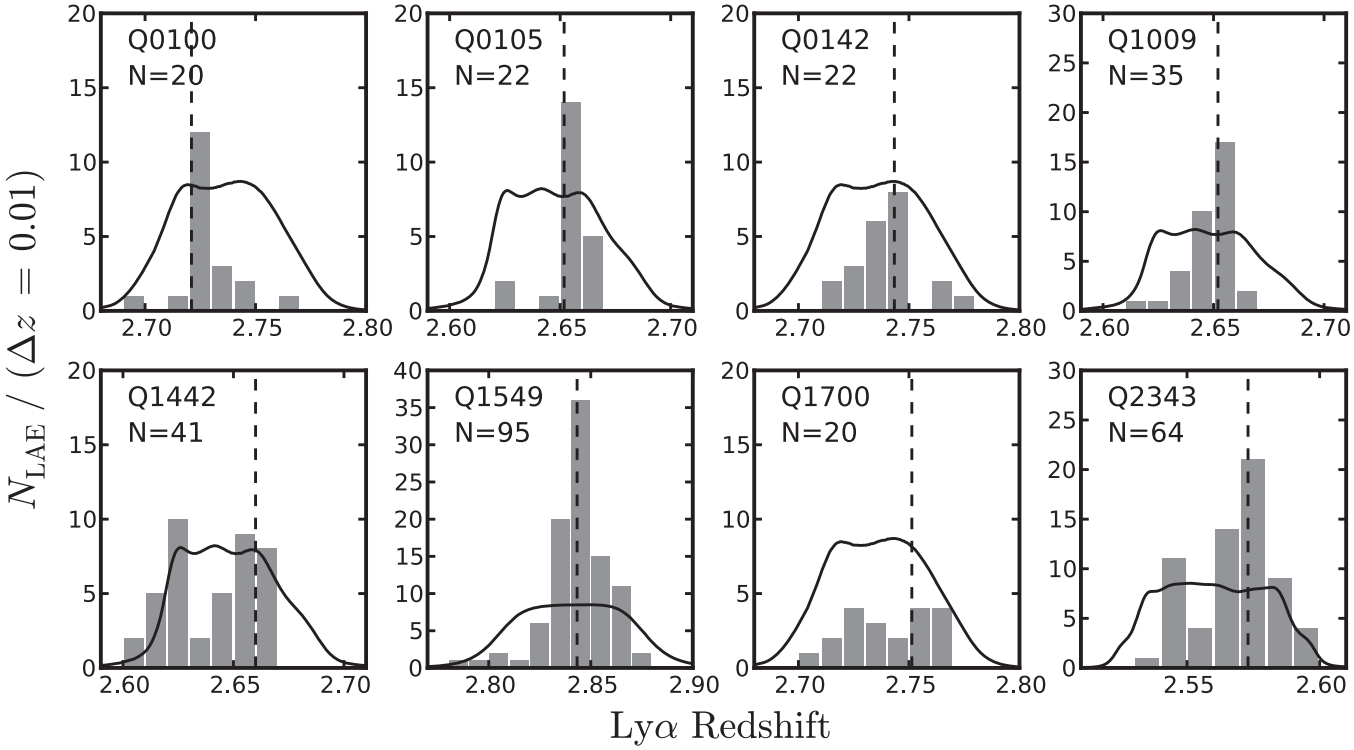

Figure 3. Redshift distribution of all spectroscopically identified LAEs in each field (gray). For each field, the number of objects with spectra is given in the upper left. Vertical dashed lines correspond to the HLQSO redshift in each field. Solid black lines denote the transmission function for the narrowband filter used to select objects in each field; the normalization is such that $N = 1$ is 10% transmission, the cut-off value for the automatic line-detection algorithm. Note that nearly all fields display a strong association of LAEs with the QSO redshift in addition to a more broadly distributed component.

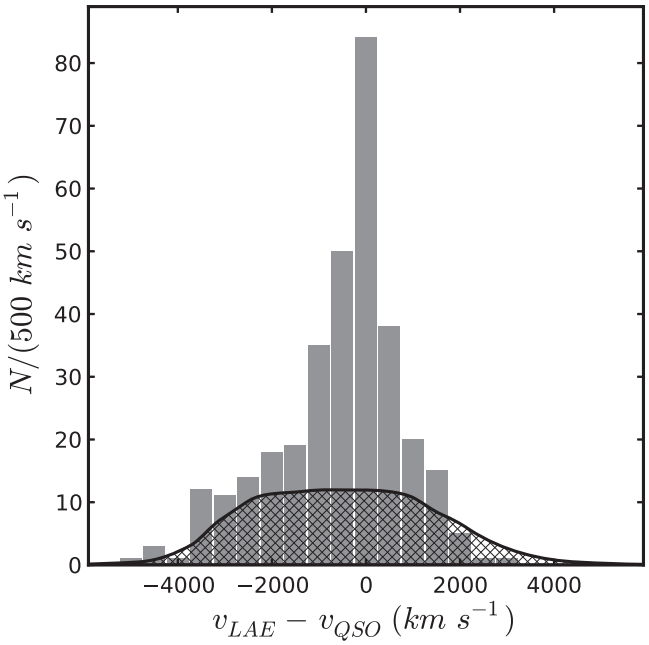

Figure 4. Velocity distribution of all spectroscopically identified LAEs with respect to their nearby hyperluminous QSO. The LAE redshifts are taken from the spectral detection of Lyα, but are shifted by -200 km s^{-1} to account for the mean Lyα offset with respect to systemic. The hatched curve is the selection function defined by the set of narrowband filters used to select the LAEs.

imaging in these fields is forthcoming. The similar LAE sample of Erb et al. (2014), however, have a median effective half-light radius $a = 0.6$ kpc in *HST* F814W photometry. Taking this value as a typical size for the KBSS-Lyα LAEs, we can estimate their dynamical masses via the formula $M_{\rm dyn} = 5a\sigma^2/G$. As in Erb et al. (2014), we assume a spherical geometry for these systems, noting that the dynamical mass would be smaller for a disk-like geometry. Further discussion of the likely physical morphologies of these objects is given in Section 4.3. For the assumed geometries and sizes, the KBSS-Lyα LAEs would have dynamical masses $1.4 \times 10^8\,M_\odot < M_{\rm dyn} < 8.4 \times 10^9\,M_\odot$.[8] The median mass is $\langle M_{\rm dyn}\rangle = 8.0 \times 10^8 M_\odot$.

3. Lyα SPECTRAL MORPHOLOGY

The observed luminosity and spectral profile of the Lyα line is the result of both the input distribution of Lyα photons produced directly from recombination and the resonant scattering that impedes and shapes their escape. The net result of these processes in star-forming galaxies is generally seen to be the broadening of the Lyα line and an overall shift redward with respect to the systemic redshift (e.g., Shapley et al. 2003), an observation that can be simply explained by outflowing gas that drives Lyα photons to significant shifts in both space and velocity (Mas-Hesse et al. 2003; Steidel et al. 2010). The scattering and absorption of these Lyα photons likewise leads to severely attenuated luminosities with respect to early predictions of star formation-associated Lyα emission (e.g., Partridge & Peebles 1967; Giavalisco et al. 1996). The details of these effects, however, depend on many factors, including

[8] With the exception of Q2343-NB2807 (for which a single Gaussian function is a poor fit to the nebular line profile), the largest estimated dynamical mass in our LAE sample is $3.7 \times 10^9\,M_\odot$. Note also that the lower mass bound does not include those objects with only an upper bound on their nebular velocity dispersion.

Table 2
MOSFIRE Observations

Object Name	$W_{Ly\alpha}$ (Å)	$z_{Ly\alpha}^{peak}$ [a]	z_H [a]	z_K [a]	$v_{Ly\alpha}^{peak}$ (km s^{-1})	$v_{Ly\alpha}^{ave}$ (km s^{-1})	σ_{neb} [b] (km s^{-1})	$\mathcal{R}$ (mag)	$F_{Ly\alpha}$ [c] (10^{-17})	$F_{H\alpha}$ [c] (10^{-17})	$F_{Ly\alpha}/F_{H\alpha}$
Q2343-NB0280	52.6	2.5801	2.5777	⋯	201	364	34 ± 9	26.6	6.4 ± 0.2	⋯	⋯
Q2343-NB0308[e]	58.8	2.5690	2.5663	(2.5666)[d]	226	360	<35	26.4	4.0 ± 0.3	1.3 ± 0.3	3.1
Q2343-NB0345	36.9	2.5917	⋯	2.5876	343	414	21 ± 6	25.3	13.2 ± 0.4	3.8 ± 0.3	3.5
Q2343-NB0405	134.8	2.5892	2.5862	(2.5860)[d]	247	293	33 ± 8	27.1	2.9 ± 0.2	1.0 ± 0.2	2.9
Q2343-NB0565	313.9	2.5661	⋯	2.5635	215	54	34 ± 12	26.8	5.7 ± 0.3	1.3 ± 0.2	4.4
Q2343-NB0791	37.4	2.5710	⋯	2.5741	−259	−116	39 ± 9	⋯	3.6 ± 0.3	2.7 ± 0.3	1.3
Q2343-NB1154	54.1	2.5773	⋯	2.5765	65	219	<35	⋯	5.8 ± 0.2	1.0 ± 0.3	5.6
Q2343-NB1174	236.6	2.5509	⋯	2.5478	262	283	<35	⋯	12.5 ± 0.4	1.5 ± 0.3	8.6
Q2343-NB1361	90.6	2.5599	2.5587	(2.5586)[d]	105	50	36 ± 8	27.0	3.4 ± 0.2	0.3 ± 0.1	11.2
Q2343-NB1386	25.8	2.5691	⋯	2.5647	371	89	<35	>27.3	1.6 ± 0.2	1.1 ± 0.3	1.5
Q2343-NB1416	20.7	2.5602	2.5582	(2.5594)[d]	169	275	35 ± 14	26.8	1.8 ± 0.2	0.7 ± 0.3	2.4
Q2343-NB1501	35.2	2.5614	2.5593	(2.5592)[d]	180	158	71 ± 12	>27.3	1.7 ± 0.2	1.2 ± 0.4	1.4
Q2343-NB1518	22.3	2.5890	⋯	2.5860	251	238	<35	26.2	3.3 ± 0.2	0.8 ± 0.3	4.0
Q2343-NB1585	303.4	2.5669	2.5649	(2.5652)[d]	169	93	<35	>27.3	5.1 ± 0.2	0.6 ± 0.2	9.0
Q2343-NB1692	359.2	2.5625	⋯	2.5602	194	85	14 ± 9	26.8	5.6 ± 0.2	1.1 ± 0.3	5.0
Q2343-NB1783	35.0	2.5784	2.5767	(2.5766)[d]	143	167	51 ± 3	25.7	7.8 ± 0.2	2.0 ± 0.2	3.8
Q2343-NB1789	88.2	2.5471	⋯	2.5448	196	59	45 ± 16	>27.3	2.3 ± 0.2	1.4 ± 0.3	1.6
Q2343-NB1806	19.3	2.5982	⋯	2.5954	237	204	73 ± 19	26.7	1.2 ± 0.1	1.4 ± 0.3	0.8
Q2343-NB1828	26.7	2.5753	⋯	2.5724	247	216	38 ± 15	26.9	2.7 ± 0.3	1.0 ± 0.2	2.6
Q2343-NB1829	32.1	2.5782	⋯	2.5754	233	271	41 ± 8	25.9	5.7 ± 0.2	2.6 ± 0.3	2.2
Q2343-NB1860	23.6	2.5740	⋯	2.5741	−11	237	<35	25.7	1.2 ± 0.2	1.0 ± 0.3	1.2
Q2343-NB2211[e]	66.2	2.5776	2.5760	(2.5758)[d]	135	206	30 ± 13	26.9	4.3 ± 0.3	1.1 ± 0.2	4.0
Q2343-NB2571	29.4	2.5820	⋯	2.5850	−249	−503	38 ± 26	>27.3	1.4 ± 0.3	0.8 ± 0.2	1.8
Q2343-NB2785	14.2	2.5723	⋯	2.5785	−517	−367	<35	>27.3	1.3 ± 0.1	0.4 ± 0.1	3.2
Q2343-NB2807[e]	24.6	2.5479	2.5446	⋯	279	184	110 ± 8	23.8	23.4 ± 0.3	⋯	⋯
Q2343-NB2816	58.5	2.5782	⋯	2.5742	340	243	57 ± 23	>27.3	2.0 ± 0.1	1.5 ± 0.4	1.4
Q2343-NB2821	32.4	2.5800	⋯	2.5779	173	69	24 ± 23	⋯	1.3 ± 0.2	1.3 ± 0.4	1.0
Q2343-NB2834	7.2	2.5700	⋯	2.5683	142	−69	<35	>27.3	0.9 ± 0.1	0.5 ± 0.2	1.7
Q2343-NB3061	57.6	2.5788	⋯	2.5764	203	270	72 ± 24	26.5	2.2 ± 0.2	2.0 ± 0.5	1.1
Q2343-NB3170	90.0	2.5488	2.5475	⋯	113	152	15 ± 5	>27.3	2.6 ± 0.1	⋯	⋯
Q2343-NB3231[f]	110.4	2.5737	2.5711	(2.5695)[d]	218	151	43 ± 12	25.9	8.4 ± 0.2	1.0 ± 0.2	8.7
Q2343-NB3292	13.4	2.5700	⋯	2.5631	579	153	<35	>27.3	1.3 ± 0.2	0.6 ± 0.2	2.2

Notes.
[a] $z_{Ly\alpha}$, z_H, and z_K denote the redshifts measured from fitting the Lyα emission line, H-band emission lines (primarily [O III] λ5007), and K-band emission lines (Hα exclusively).
[b] σ_{neb} is the velocity width of the nebular emission line used to define z_{neb}. Both the line widths and their associated uncertainties reflect the deconvolution of the $\sigma_{inst} = 35$ km s^{-1} instrumental profile.
[c] Line fluxes (in cgs units) are determined from a combination of spectroscopic and photometric measurements as described in Section 3.2.
[d] In the nine cases where both the H-and K-band spectra yielded redshifts, we adopted the higher-S/N H-band redshifts to define z_{neb}.
[e] The nebular redshifts of Q2343-NB0308, Q2343-NB2211, and Q2343-NB2807 were measured from the [O III] λ4959Å line because the λ5007Å line did not fall on the detector.
[f] The nebular redshift of Q2343-NB3231 was measured from the Hβ line (and cross-checked with Hα) because the [O III] λ5007Å and λ4959Å lines did not fall on the detector.

the dust content, column density, covering fraction, and velocity distribution of the scattering medium.

As the Lyα line profile bears the imprint of these diverse galaxy and gas properties, it is an important tool for studying galaxy evolution. However, the degenerate effects of these processes require care in their interpretation. For instance, Hashimoto et al. (2013), Schenker et al. (2013), and Shibuya et al. (2014) show that galaxies selected via their Lyα emission have a smaller velocity shift of Lyα with respect to systemic compared to continuum-selected galaxies (e.g., those of Steidel et al. 2010). Erb et al. (2014) extend this study to a large sample of LAEs and LBGs with systemic redshifts, demonstrating that the Lyα velocity shift shows a significant inverse trend with $W_{Ly\alpha}$ for the combined population of galaxies selected by either technique. The physical basis of this relationship remains unclear, however. In particular, it is not clear whether the velocity offset of Lyα is predominantly driven by outflow velocity (as suggested by Hashimoto et al. 2013) or H I optical depth (as suggested by Chonis et al. 2013).

Furthermore, many LAEs do not exhibit simple Lyα shifts, but rather show complex, multi-peaked profiles that may correspond to either internal star formation (Kulas et al. 2012) or externally illuminated fluorescent processes (Kollmeier et al. 2010). In particular, Lyα lines that are *blueshifted* with respect to systemic are predicted by simple models of emission from inflowing H I (Verhamme et al. 2006) whose low star formation and intrinsic Lyα-production would likely hide them from view in non-fluorescing populations. The distribution of Lyα spectral properties and their relation to other physical properties of the galaxies (including the Lyα escape fraction) are thus an important window into the processes that drive gas into and out of galaxies throughout their evolution.

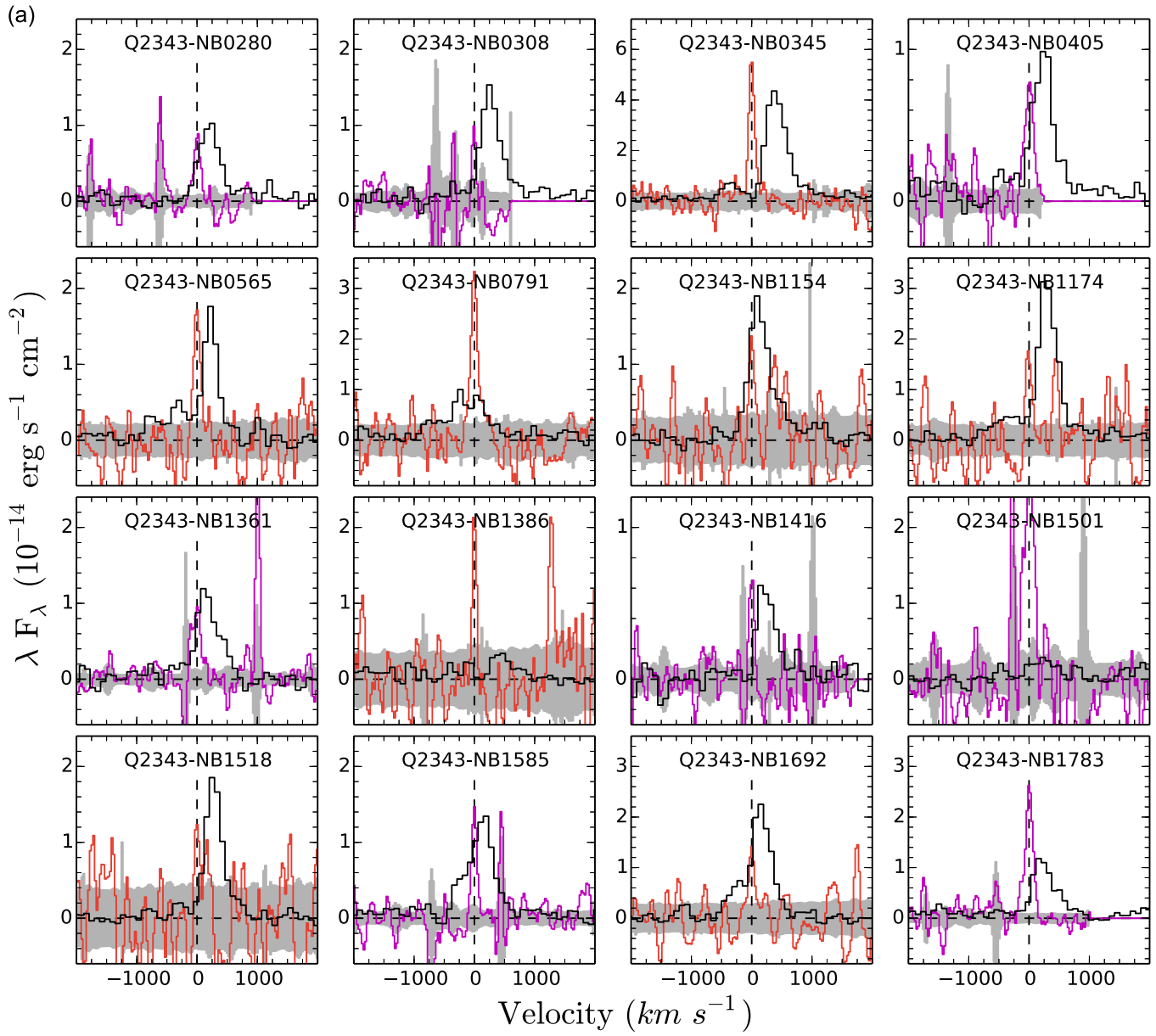

Figure 5. (a) Lyα and nebular line spectra for the subsample of objects with MOSFIRE redshifts. Lyα spectra (black) are from LRIS, with resolution $R \sim 1300$. Nebular spectra are for the Hα line (K band, red) or Hβ or [O III] (H band, purple), whichever was used to estimate the systemic redshift (see Table 2 and notes below). MOSFIRE spectra have been smoothed by a three-pixel boxcar to reduce noise. Gray regions denote the $\pm 1\sigma$ uncertainties on the MOSFIRE spectra. Both spectra are shifted to the redshift frame estimated from $z_{\rm neb}$. The fluxes are in λF_λ units to facilitate comparison of their integrated line luminosities. (b) Spectra for the remainder of the MOSFIRE LAE sample.

3.1. Lyα Escape Fraction

Postage stamps of each Lyα and nebular line spectrum in the MOSFIRE sample are displayed in Figure 5. The majority of the nebular redshifts are derived from Hα, for which the intrinsic flux ratio is $F_{\rm Ly\alpha}/F_{\rm H\alpha} \approx 8.7$ under the typical assumption of case-B (i.e., ionization-bounded) recombination and $T_e = 10^4$ K.[9]

The LAE Lyα line fluxes ($F_{\rm Ly\alpha}$) are measured photometrically from their continuum-subtracted narrowband detections. Directly integrating the rest-UV spectrum yields a Lyα flux $\sim 2\times$ smaller on average. This difference may be partially due to uncertainties in the absolute flux calibration of the rest-UV spectra, but the consistency between our stacked continuum spectra and broadband flux measurements (Section 4.1) suggests that this effect is minimal. Similarly, the photometric errors in the measured narrowband Lyα fluxes are estimated to be $\lesssim$15%. Rather, it appears that the differential slit losses between Lyα and continuum photons are significant within our $1\farcs2$ wide slits.

For the MOSFIRE subsample of LAEs with K-band spectra, Hα fluxes ($F_{\rm H\alpha}$; Table 2) are estimated by a Gaussian fit to the emission line. Slit losses are difficult to estimate for individual faint objects, so the measured values have been multiplied by a

[9] The assumed ratio $F_{\rm Ly\alpha}/F_{\rm H\alpha} \approx 8.7$ is commonly adopted in the literature, often with reference to Brocklehurst (1971). However, Brocklehurst (1971) does not explicitly calculate $F_{\rm Ly\alpha}/F_{\rm H\alpha}$, but only line ratios including states at energy levels $n \geq 2$ (e.g., Hα/Hβ; see note in Henry et al. 2015). While there is some variation in the calculated Lyα/Hβ and Hα/Hβ ratios with temperature and density (e.g., Dopita & Sutherland 2003), values in the range $F_{\rm Ly\alpha}/F_{\rm H\alpha} = 8$–10 are typical and do not change our results appreciably. We adopt $F_{\rm Ly\alpha}/F_{\rm H\alpha} \approx 8.7$ for consistency with previous studies at high and low redshifts (e.g., Hayes et al. 2010; Henry et al. 2015).

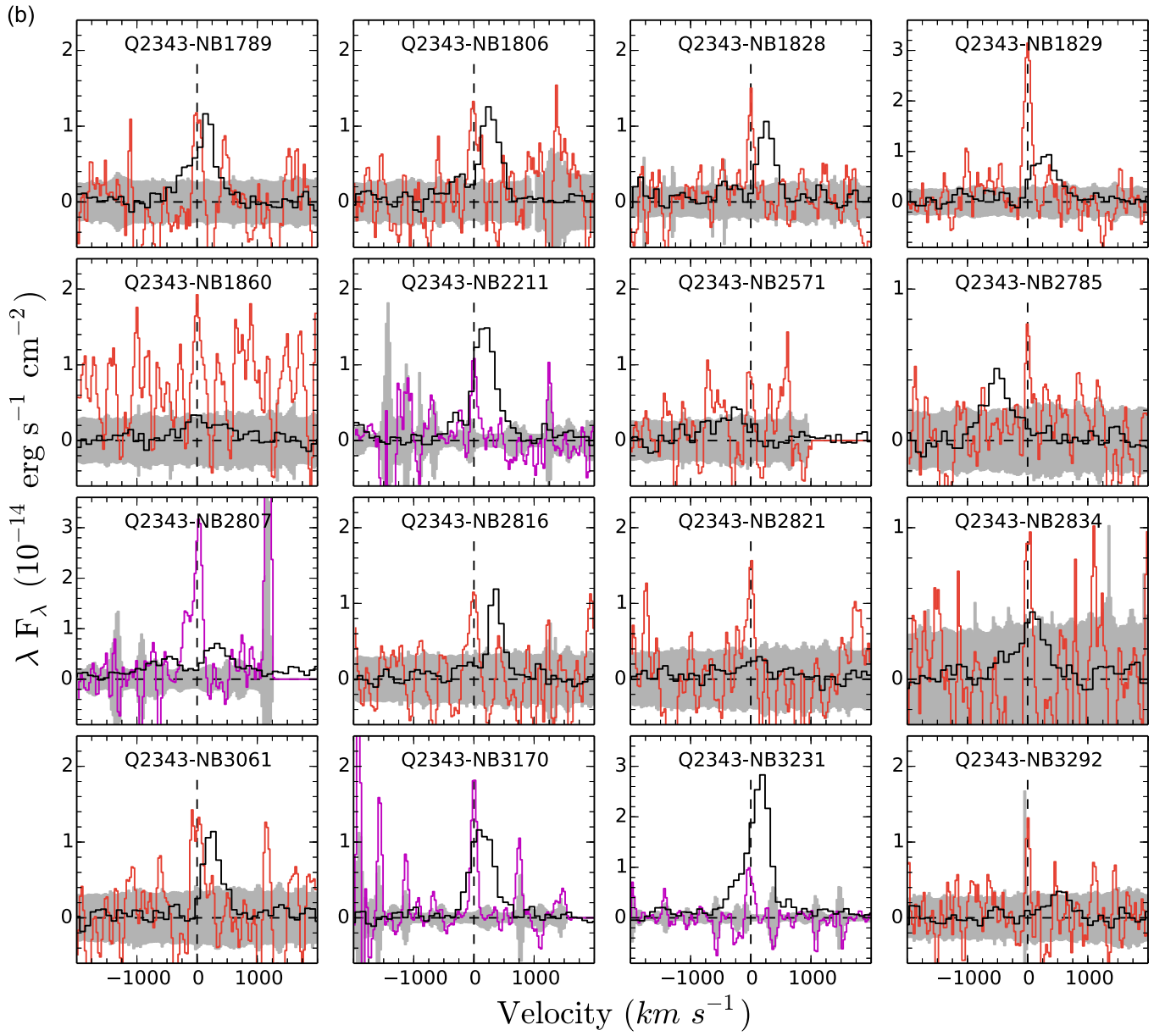

Figure 5. (Continued.)

factor 1.5–2.1 (depending on the mask) to account for the average slit loss measured for bright point sources on the same slitmasks (A. Strom et al. 2015, in preparation). Most LAEs in our sample do not have robust detections of both Hα and Hβ, so we have not corrected the Hα fluxes for dust attenuation, but the four objects with Hα and Hβ S/N > 2 have a mean ratio $\langle F_{\rm H\alpha}/F_{\rm H\beta}\rangle = 3.3 \pm 1.1$, consistent with the canonical (non-attenuated) case-B value $F_{\rm H\alpha}/F_{\rm H\beta} = 2.86$ (Brocklehurst 1971).

The measured line ratios in Figure 5 vary considerably ($F_{\rm Ly\alpha}/F_{\rm H\alpha}\sim$ 1–11, Table 2) with respect to that predicted by case-B recombination. If the intrinsic $F_{\rm Ly\alpha}/F_{\rm H\alpha}$ flux ratio is assumed to be 8.7 (and the Hα flux is not significantly affected by extinction), then the median ratio $\langle F_{\rm Ly\alpha}/F_{\rm H\alpha}\rangle = 2.7$ suggests a typical Lyα escape fraction $\langle f_{\rm esc,Ly\alpha}\rangle = \langle F_{\rm Ly\alpha}^{\rm observed}/F_{\rm Ly\alpha}^{\rm intrinsic}\rangle \approx 30\%$. This $F_{\rm Ly\alpha}/F_{\rm H\alpha}$ ratio is consistent with that observed in the 4 objects with Hα line detections in the similar faint-LAE sample of Erb et al. (2014). If the Hα emission is attenuated by interstellar dust, then the intrinsic values of $f_{\rm esc,Ly\alpha}$ may be lower, but the measured values are considerably higher than previous estimates of $f_{\rm esc,Ly\alpha} \approx 5\%$ for typical high-redshift star-forming galaxies (Hayes et al. 2010; Steidel et al. 2011; Ciardullo et al. 2014). Such high Lyα escape fractions are suggestive of the high LyC escape fractions observed in samples of LAEs (Mostardi et al. 2013; Nestor et al. 2013) and may indicate low H I optical depths for photons escaping from star-forming regions in these galaxies. Given the proximity of these LAEs to HLQSOs, however, it may be that $f_{\rm esc,Ly\alpha}$ is elevated by the "fluorescent" boosting of the total Lyα flux from these objects.

For comparison, the KBSS LBGs have a median flux ratio $\langle F_{\rm Ly\alpha}/F_{\rm H\alpha}\rangle \approx 0.5$, or a corresponding escape fraction $f_{\rm esc,Ly\alpha} \approx 6\%$. The LBG H$\alpha$ slit losses were corrected in a similar manner to the LAEs, and further analysis of the rest-frame optical spectra of the KBSS LBGs will be presented in

A. Strom et al. (2015, in preparation). The LBGs lack narrowband Lyα photometry, so the Lyα fluxes were measured by direct integration of the rest-UV spectrum (after flux-calibrating the spectrum based on the broadband G-band flux). Steidel et al. (2011) measure Lyα aperture corrections for LBG spectra showing Lyα in net emission or absorption in comparison to LAEs, finding that LBGs with detected Lyα emission show similar differential slit losses to LAEs in our 1.″2 slits. In this case the Lyα luminosities of the KBSS LBGs may be underestimated by a factor of $\sim 2\times$, and the escape fractions may be $f_{\rm esc,Ly\alpha} \approx 12\%$ in a larger aperture. This Lyα escape fraction is similar to that derived for Lyα-emitting LBGs ($f_{\rm esc,Ly\alpha} = 14.4\%$) by Steidel et al. (2011). It thus appears that our sample of Lyα-emitting, continuum-color selected KBSS LBGs have a broadly similar Lyα escape fraction with respect to previously studied samples of LBGs, and significantly smaller values than the KBSS-Lyα LAEs.

Given the small number of LAEs with Hα detections, it is difficult to investigate trends within the MOSFIRE LAE sample. In particular, we find no association between $f_{\rm esc}$ and the Lyα offset, peak multiplicity, or peak separation ($v_{\rm Ly\alpha}$, $f_{\rm mult}$, and $v_{\rm peaks}$; see discussion in Sections 3.2–3.3). However, we find a significant trend between $f_{\rm esc,Ly\alpha}$ and $W_{\rm Ly\alpha}$, which are positively correlated with $p < 4 \times 10^{-3}$ for a Pearson correlation test. This result suggests that $W_{\rm Ly\alpha}$ is primarily an indicator of Lyα *escape*, not Lyα *production* among these faint galaxies. In fact, the relation between Hα luminosity (a standard indicator of SFR) and $W_{\rm Ly\alpha}$ is weakly negative in the sample. Given that a higher $W_{\rm Ly\alpha}$ at a given observed Lyα luminosity corresponds to a fainter UV continuum luminosity (another proxy for SFR), we suggest that $W_{\rm Ly\alpha}$ is likely *anti-correlated* with SFR among these faint LAEs. This effect is similar to the anti-correlation observed between $W_{\rm Ly\alpha}$ and UV SFR (or luminosity) seen in several previous studies (e.g., Ando et al. 2006; Ouchi et al. 2008; Kornei et al. 2010; Stark et al. 2010; Atek et al. 2014). We also find a tentative, negative association between $W_{\rm Ly\alpha}$ and $\sigma_{\rm neb}$ (the width of the nebular Hα and/or [O III] emission). Because $\sigma_{\rm neb}$ traces the stellar velocity dispersion and thus the dynamical mass of the galaxy, this may suggest that higher $W_{\rm Ly\alpha}$ is associated with lower dynamical masses. However, further study of the stellar populations and SFRs of the LAEs (including our ongoing photometry and rest-frame optical spectroscopy of these objects) will be necessary to confirm the physical basis of these trends.

3.2. Velocity Shift with Respect to Systemic Redshift

The offset of the Lyα line with respect to the systemic redshift was measured for each of the 32 LAEs in the MOSFIRE sample using the $z_{\rm Ly\alpha}$ and $z_{\rm neb}$ values estimated as described in Sections 2.2 and 2.3. The velocity offset was then inferred from the measured redshifts as

$$v_{\rm Ly\alpha} = \frac{z_{\rm Ly\alpha} - z_{\rm neb}}{1 + z_{\rm neb}} c. \quad (4)$$

The velocity shift of the Lyα line with respect to the systemic redshift is clear from the panels in Figure 5. The majority (28/32; 88%) of spectra display the redshifted Lyα profile typical of star-forming galaxies, but there are several objects with minimal velocity shift, or even a dominant peak blueward of the systemic redshift. The distribution of measured velocity shifts (Equation (4)) is given in Figure 6.

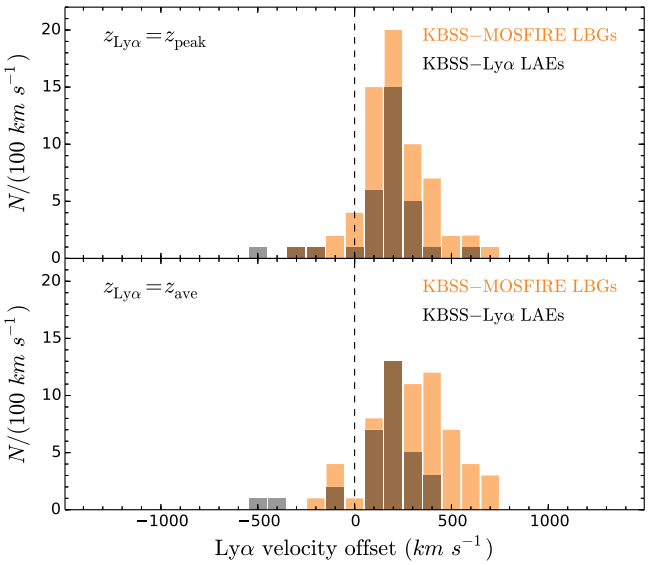

Figure 6. Distribution of Lyα velocity offsets with respect to systemic for LAEs (gray) and KBSS LBGs (orange) with nebular redshifts measured with MOSFIRE. In each panel, the vertical dashed line denotes $v_{\rm Ly\alpha} = 0$. Top: the distributions when $z_{\rm Ly\alpha}$ is defined by the peak of the fit line profile ($z_{\rm Ly\alpha,peak}$). Most of the galaxies have offsets in a tight range around $v_{\rm Ly\alpha} = 200$ km s^{-1}, but a few LAEs have Lyα lines blueshifted with respect to the systemic redshift ($v_{\rm Ly\alpha} < 0$). Bottom: the distributions when $z_{\rm Ly\alpha}$ is defined by the line centroid ($z_{\rm Ly\alpha,ave}$). Most LAEs have $v_{\rm Ly\alpha} \sim 200$ km s^{-1}, but with a broader distribution compared to the $z_{\rm Ly\alpha} = z_{\rm peak}$ distribution. The LBG centroid velocities occupy a broader, more highly redshifted range than either the LAEs or the corresponding LBG Lyα peaks.

The typical Lyα shift of $+200$ km s^{-1} is clearly visible. This shift is consistent with that found for the few samples of LAEs with systemic redshifts in the literature (e.g., McLinden et al. 2011; Chonis et al. 2013; Hashimoto et al. 2013; Shibuya et al. 2014), and significantly less than that previously measured in samples LBGs (300–400 km s^{-1}, Steidel et al. 2010). However, we demonstrate below that the detailed velocity distribution depends on the method by which the Lyα emission redshift is assigned.

The two panels of Figure 6 show the effect of defining $z_{\rm Ly\alpha}$ by either the fitted peak ($z_{\rm Ly\alpha,peak}$) or the flux-weighted centroid of the line profile ($z_{\rm Ly\alpha,ave}$; see Section 2.2). Both methods yield qualitatively similar distributions, with median values $\langle v_{\rm Ly\alpha,peak} \rangle = 198$ km s^{-1} and $\langle v_{\rm Ly\alpha,ave} \rangle = 176$ km s^{-1}. However, $z_{\rm Ly\alpha,peak}$ displays a tighter correlation with the redshift derived from nebular emission lines than $z_{\rm Ly\alpha,ave}$. The median absolute deviations (a scale estimator that is insensitive to outliers) of the two distributions of $v_{\rm Ly\alpha}$ are ${\rm MAD}(v_{\rm Ly\alpha,peak}) = 54$ km s^{-1} and ${\rm MAD}(v_{\rm Ly\alpha,ave}) = 93$ km s^{-1}. The similarities between the two distributions suggest that either quantity is a reasonable proxy for the systemic redshift after correcting for the typical 200 km s^{-1} offset, and even the individual velocities computed by both measurements are consistent within 100 km s^{-1} for the majority of objects (Table 2). Because $z_{\rm Ly\alpha,peak}$ tracks $z_{\rm neb}$ more tightly, however, we adopt $z_{\rm sys,Ly\alpha} = z_{\rm Ly\alpha,peak} - 200$ as the best estimate of the systemic redshift in the absence of nebular emission line measurements.

The distribution of Lyα line offsets from the comparison KBSS LBG sample is also displayed in Figure 6, and there the differences between the two Lyα redshift estimators are more apparent. While the distribution of fit peak velocities $v_{\rm Ly\alpha,peak}$

is again sharply peaked around $v_{\mathrm{Ly}\alpha} \approx 200\,\mathrm{km\,s^{-1}}$, the centroid velocities $v_{\mathrm{Ly}\alpha,\mathrm{ave}}$ are more extended, particularly toward higher (more strongly redshifted) velocities. The median velocity offsets for the LBG sample are $\langle v_{\mathrm{Ly}\alpha,\mathrm{peak}}\rangle = 205\,\mathrm{km\,s^{-1}}$ and $\langle v_{\mathrm{Ly}\alpha,\mathrm{ave}}\rangle = 306\,\mathrm{km\,s^{-1}}$. Note that our measurement of $v_{\mathrm{Ly}\alpha,\mathrm{peak}}$ in particular suggests a significantly smaller Lyα offset than previous studies of LBGs. Qualitatively, the difference between the two distributions is due to the fact that the LBG Lyα emission lines have extended red tails (often combined with continuum flux levels that are higher on the red side of Lyα than the blue side) that draw the velocity centroid to higher/redder values. Fitting the Lyα emission line with a symmetric Gaussian model will likewise cause the fit emission-line center to be redder than the Lyα emission peak. While the LAE emission lines tend to be asymmetric as well, they typically have more symmetric profiles and/or stronger blue secondary peaks that compensate for the extended red wing. The LAEs also have less continuum emission that is more symmetric about the wavelength of Lyα than typical LBGs (e.g., the observed ratio of f_{1125} to f_{1325}; see Section 4.3). The distributions of emission line widths, asymmetry, and peak multiplicity for each sample are discussed in Section 3.3 below.

Despite their differing line morphologies and photometric properties, it is significant that both the LAE and LBG samples have Lyα emission line peaks that are well-described by a uniform offset of $\sim$200 km s^{-1} redward of the systemic redshifts. While the measured velocity of the Lyα peak may be strongly dependent on spectral resolution, its constancy across a broad range of galaxy luminosities suggests that it is less sensitive to galaxy properties than the Lyα emission centroid. For a sample of galaxies observed *with the same spectral resolution*, therefore, the Lyα emission peak appears to be a robust redshift indicator across a diverse range of galaxy types (with the caveat that $\sim$50% of $z \sim 2.4$ LBGs have no net Lyα emission in their spectra; Steidel et al. 2011). We use this redshift calibration to create composite LAE spectra from our large sample of LAEs without nebular redshift measurements in Section 4.

In addition to the distribution of average or peak Lyα line velocities, it is interesting to compare the full velocity distributions of Lyα and nebular emission. Figure 7 displays the stacked Lyα and nebular line profiles of the 32 MOSFIRE LAEs. Of particular note is the breadth of the Lyα line with respect to the nebular line profile; assuming that the Lyα photons are generated by recombination processes in the same H II regions that generate the nebular emission, the top panel of Figure 7 clearly displays the diffusion of the Lyα photons in velocity as they resonantly scatter through the surrounding H I gas. Fitting a Gaussian function to the stack of nebular lines yields a velocity width of $\sigma_{\mathrm{neb}} = 35 \pm 3\,\mathrm{km\,s^{-1}}$. The stacked Ly$\alpha$ profile has a width of $\sigma_{\mathrm{Ly}\alpha} = 115 \pm 8\,\mathrm{km\,s^{-1}}$ for the primary (red) peak. These figures reflect the deconvolution of the instrumental resolution of MOSFIRE ($\sigma_{\mathrm{inst}} = 35\,\mathrm{km\,s^{-1}}$) and LRIS ($\sigma_{\mathrm{inst}} = 100\,\mathrm{km\,s^{-1}}$) in their observed modes.[10] The peak of the stacked Lyα spectrum is again quite close to $+200\,\mathrm{km\,s^{-1}}$, but there is a distinct component blueward of the systemic redshift as well. After subtracting the faint continuum, the fraction of Lyα line flux emitted with $v < 0$ is 16%. For comparison, we show the effective profile that would result from stacking all the Lyα lines at the redshifts derived from the Lyα line peak and then making a $+200\,\mathrm{km\,s^{-1}}$ shift in the bottom panel of Figure 7. The resulting profile is narrower ($\sigma_{\mathrm{Ly}\alpha} = 85 \pm 8\,\mathrm{km\,s^{-1}}$), with only 11% of the line flux emitted at $v < 0$, roughly 2/3 the flux measured using the true systemic redshifts.

[10] Note that the fits to the composite line profiles yield similar (though not identical) values to the averages of the individually fit lines (Table 3).

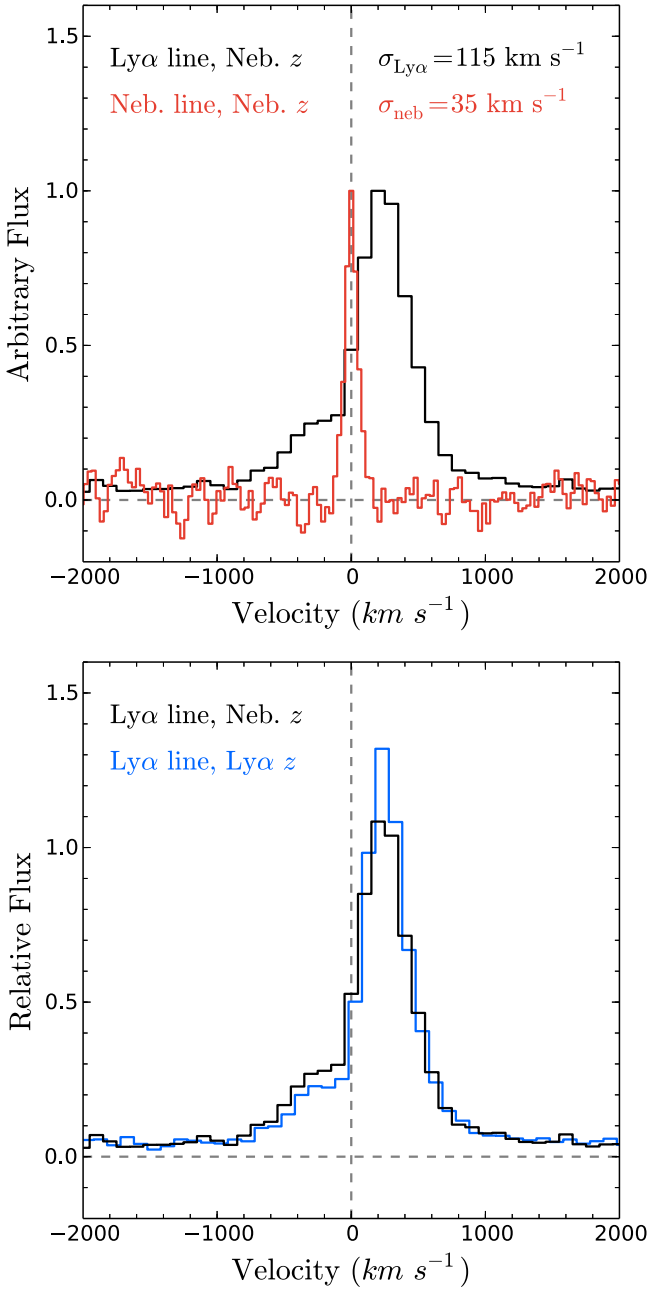

Figure 7. Stacked spectral profiles for the 32 LAEs with systemic (nebular) redshift measurements. Top: comparision of the stacked nebular (red) and Lyα (black) line profiles for these LAEs. The nebular stack consists of all measured nebular lines (Hα, Hβ, and/or [O III] $\lambda\lambda$ 4959,5007) for each LAE. The lines are stacked according to their corresponding nebular redshifts, and the effect of resonant scattering on escaping Lyα photons is clearly visible, as is the typical Lyα velocity offset of $\sim$+200 km s^{-1} relative to systemic. Bottom: comparison of the average Lyα profiles when spectra are stacked according to their nebular, systemic redshift (black, as above) and a redshift derived directly from the Lyα line peak (blue, shifted +30 km s^{-1} for clarity), wherein the "systemic" redshift is estimated as $v_{\mathrm{sys,Ly}\alpha} = v_{\mathrm{Ly}\alpha} - 200\,\mathrm{km\,s^{-1}}$. Stacking via the Ly$\alpha$ redshift distorts the Lyα profile and diminishes the measured flux blueward of the systemic redshift.

The four MOSFIRE LAEs with $v_{\mathrm{Ly}\alpha} < 0$ compose an extremely interesting, though small, group of objects. Further analysis of this sample is ongoing, including spectroscopy and photometry to constrain the stellar contribution to the LAE luminosity, enrichment, and dynamics. While only three of these blueshifted LAEs currently have $\mathcal{R}$ photometry, their average flux in that band is $\sim 1/2\times$ that of the LAEs with redshifted Lyα lines, tentatively suggesting that blueshifted LAEs have physical properties that are distinct from typical LAEs. Other properties associated with redshifted or blueshifted Lyα emission are discussed in the context of multi-peaked Lyα emission below.

3.3. Multi-peaked and Asymmetric Lyα Profiles

As discussed above, star-forming galaxies are often associated with multi-peaked Lyα emission. In a systematic study of Lyα emission among $\sim$1500 star-forming galaxies at $z \sim 2$–3, Kulas et al. (2012) found that $\sim$30% are multi-peaked, with some dependence on the spectral resolution and S/N of the observations. While most of these galaxies were observed at lower resolution, a subsample of their spectra were obtained with the same 600-line grism of Keck/LRIS used for our LAE sample and have similar integration times ($\sim$1.5 hr). This subsample included 44 multi-peaked spectra, a multiplicity rate of 27%.

Yamada et al. (2012a) studied the Lyα peak morphologies of 91 LAEs at $z \sim 3$ at similar resolution ($R \sim 1700$), finding a $\sim$50% multiplicity rate. This heterogeneous sample contains 12 Lyα-blobs from Matsuda et al. (2004), as well as compact, faint LAEs similar to those of the KBSS-Lyα sample (although with a limiting Lyα flux $\sim 2\times$ brighter, according to Yamada et al. 2012b).

For the KBSS-Lyα sample of this paper, multi-peaked systems were identified as described in Section 2.2. Of the 318 unique spectroscopically identified LAEs, 129 are found to be multi-peaked, for a multiplicity fraction of 40%. The criteria for identifying a secondary peak were not identical to that of Kulas et al. (2012); in particular, the significance threshold was not dependent on the magnitude or S/N of the primary peak, and no minimum peak separation was enforced. However, we found that adjusting the multiplicity criteria to match those of Kulas et al. as closely as possible did not significantly affect the overall rate of selection nor the spectral/physical properties of the selected sample.

Previous studies of Lyα kinematic multiplicity (among samples with or without systemic redshifts) typically group these lines into blue-peak dominant or red-peak dominant lines, motivated by the association of blue (red) peak dominance with inflowing (outflowing) gas in radiation transfer models (e.g., Zheng & Miralda-Escudé 2002; Dijkstra et al. 2006; Verhamme et al. 2006). Kulas et al. (2012) found that 67% of their 239 multi-peaked objects (the majority of which had lower spectral resolution than the KBSS-Lyα sample) have dominant red peaks. A selection of examples of the diverse Lyα spectral morphologies represented among the KBSS-Lyα LAEs is displayed in Figure 8, and the distribution of red/blue peak dominance in our sample is displayed in Figure 9. In the top panel of Figure 9, we show the distribution of inter-peak velocities, defined as $\Delta v_{\mathrm{peaks}} = c(z_{\mathrm{peak,pri}} - z_{\mathrm{peak,sec}})/(1 + (z_{\mathrm{peak,pri}})$. $z_{\mathrm{peak,pri}}$ is the redshift of the first peak identified by the line detection algorithm discussed in Section 2.2 (i.e., the peak of the asymmetric Gaussian profile fit to the highest peak in the smoothed spectrum), and $z_{\mathrm{peak,sec}}$ is the redshift corresponding to the mean of the second fit Gaussian component. For this definition, $\Delta v_{\mathrm{peaks}} > 0$ corresponds to red-dominant systems, such that the primary peak is redward of the inter-peak trough.

Of the 129 multi-peak LAEs, 96 (74%) have dominant red peaks ($\Delta v_{\mathrm{peaks}} > 0$), while 33 (26%) are blue dominant ($\Delta v_{\mathrm{peaks}} < 0$; Table 3). The red-dominant LAEs have a quite narrow distribution of peak separations, with a median value $\langle \Delta v_{\mathrm{peaks}} \rangle = 560\ \mathrm{km\ s^{-1}}$ and a standard deviation $\sigma(\Delta v_{\mathrm{peaks}}) = 220\ \mathrm{km\ s^{-1}}$. Conversely, the blue-dominant LAEs have a larger velocity shift over a broader range: $\langle \Delta v_{\mathrm{peaks}} \rangle = -660\ \mathrm{km\ s^{-1}}$ and $\sigma(\Delta v_{\mathrm{peaks}}) = 300\ \mathrm{km\ s^{-1}}$. A similar contrast can be seen in the flux distribution within these multi-peaked LAEs (Figure 9, bottom panel). The fraction of total Lyα flux in the red peak, $F_{\mathrm{red}}/F_{\mathrm{tot}}$, is defined as the integral of the redder of the two Gaussian components divided by the integral of the sum of the two components. There are 101 LAEs (78%) with $F_{\mathrm{red}}/F_{\mathrm{tot}} > 0.5$, an alternative definition of red-peak dominance. The sets of LAEs with $\Delta v_{\mathrm{peaks}} > 0$ and $F_{\mathrm{red}}/F_{\mathrm{tot}} > 0.5$ overlap almost entirely,[11] but we use the prior definition (based on the significance of peaks in the smoothed spectrum) for consistency with Kulas et al. (2012) and other surveys that assume different model profiles.

Due to the presence of nearby HLQSOs in these LAE fields, it is important to discern what role the external illumination of the QSO (i.e., "fluorescence") may play in shaping the observed spectral morphology of the LAEs. Clearly, the fluorescing LAEs must inhabit the region of the environment illuminated by the QSO in order for the ionizing field to have an observable effect. As argued in Trainor & Steidel (2013), the combination of geometry and the finite QSO lifetime (measured to be $\lesssim$20 Myr) cause this fluorescence to be observable only when the LAE is in the foreground of the QSO, or less than $\sim 10^7$ lightyears (3.2 proper Mpc) distant in the background.

The redshift distribution relative to the QSOs of all the multi-peaked LAEs is shown in Figure 10. Care must be taken in comparing the redshift distributions of red- and blue-dominant LAEs based on the redshifts of their Lyα lines. Figure 10 shows the redshift distribution when the systemic redshift of each LAE is taken to be $200\ \mathrm{km\ s^{-1}}$ blueward of the red Lyα peak, *regardless of whether the redder peak is primary or secondary*. The redshift distribution of red-dominant Lyα profiles is fairly symmetric, with a slight bias toward the QSO foreground. The blue-dominant LAEs, however, show a strong association with the region in the immediate background of the QSO. A two-sample KS test finds only a small ($p \approx 0.03$) likelihood of both samples being drawn from the same distribution.

Given the uncertainty in assigning redshifts to those sources without accurate systemic redshifts from optically thin nebular emission lines, it is unclear whether the blue-dominant LAEs are localized within the QSO field, or whether they differ from the red-dominant distribution at all. As noted above, blueshifted Lyα emission is a possible observational signature of infalling gas illuminated by a central source. Given the proximity of the HLQSOs, however, it is also possible that the detected emission has a significant fluorescent contribution.

[11] The small number of objects with $F_{\mathrm{red}}/F_{\mathrm{tot}} > 0.5$ and $\Delta v_{\mathrm{peaks}} < 0$ (or vice versa) generally have a secondary peak that was fit with a broad Gaussian profile, thereby including more total flux despite having a lower S/N.

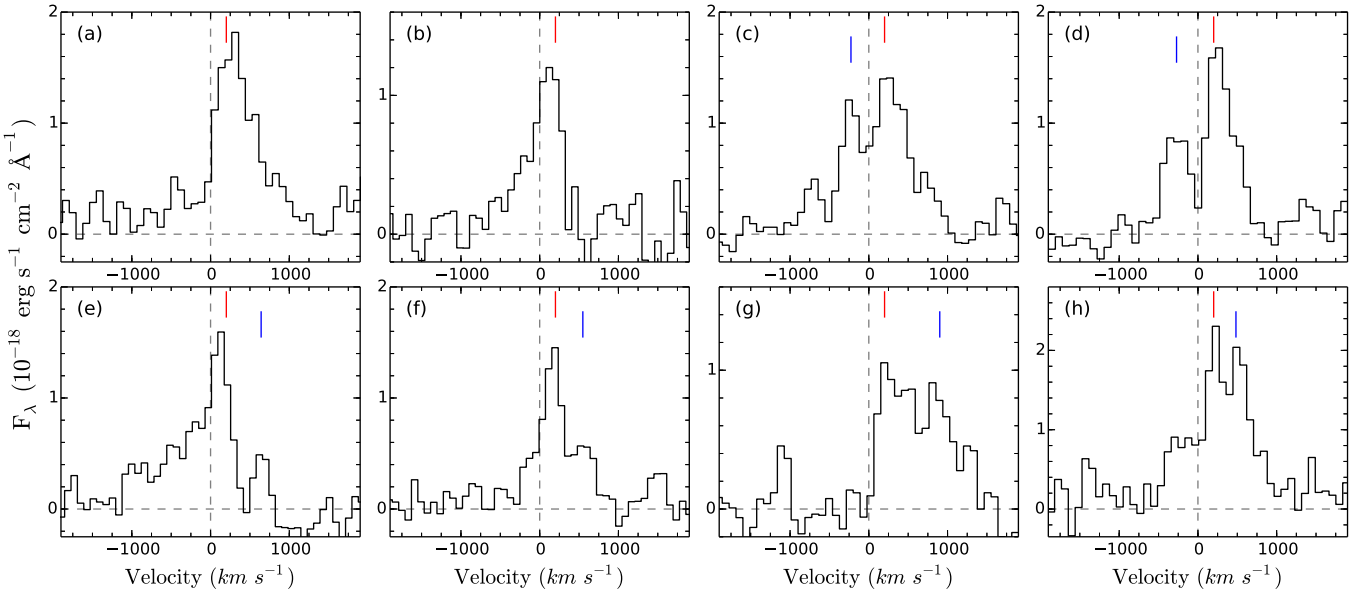

Figure 8. Sample of the diverse Lyα spectral morphologies represented within our spectroscopic sample of LAEs. Red vertical lines denote the redshift fit to the primary Lyα peak by our algorithm, while blue vertical lines denote the fit position of the secondary peak (when detected with significance). Redshifts are assigned to be -200 km s^{-1} with respect to the primary Lyα peak. The top row (panels (a)–(d)) includes examples of common morphological types: single-peaked lines with red (a) or blue (b) asymmetric tails, or double-peaked lines with dominant red peaks (c), (d). The bottom row (panels (e)–(f)) shows examples of the less common blue-dominant double-peaked lines. Despite their similar peak ratios, panels (e) and (f) have extended blue tails, whereas panels (g) and (h) have extended red tails.

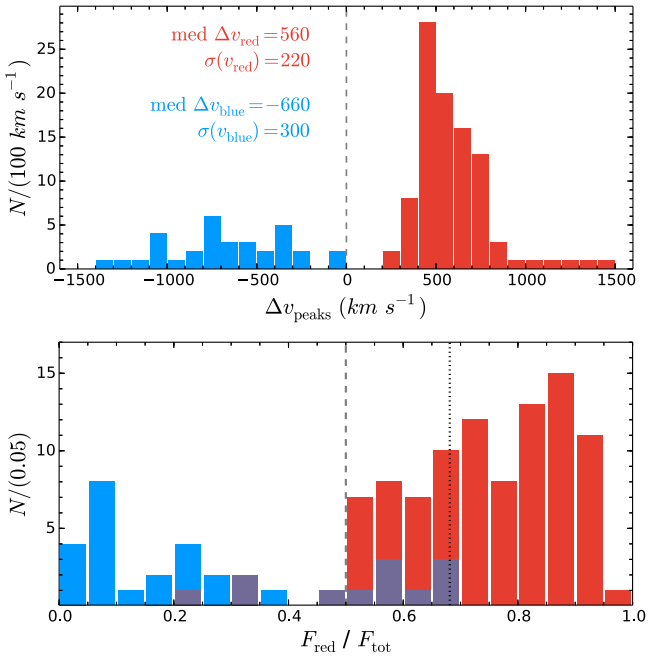

Figure 9. Top: distribution of peak separations among the 129 LAEs with identified multi-peaked Lyα emission lines (40% of the 318 LAEs with Lyα spectra). The majority (96/129) have dominant red peaks ($\Delta v > 0$, red), but a substantial minority (33/129) have dominant blue peaks ($\Delta v < 0$, blue). The dashed gray line denotes $\Delta v = 0$. The red-peak-dominant systems have a smaller median peak separation (560 vs. 660 km s^{-1}) than the blue-peak-dominant systems, as well as a smaller scatter about this value (220 vs. 300 km s^{-1}). Bottom: the distribution (stacked histogram) of flux in the red peak (F_{red}) as a fraction of total Lyα flux (F_{tot}) for the same 129 multi-peaked LAEs, with colors matched to the top panel. Red-peak-dominant Lyα lines (red, $\Delta v > 0$ in the top panel) generally have $F_{red}/F_{tot} > 0.5$, and the median flux ratio among all systems is $F_{red}/F_{tot} = 0.68$ (dotted black line).

Table 3
LAE and LBG Emission-line Properties

	LAEs	MOSFIRE LAEs[a]	KBSS LBGs
N_{obj}	318	32	65
$\langle F_{Ly\alpha} \rangle$[b] ($10^{-17}$ cgs)	4.5 ± 0.8	4.6 ± 0.8	7.3 ± 1.6
$\langle \sigma_{Ly\alpha} \rangle$ (km s^{-1})	144 ± 3	138 ± 8	195 ± 7
N_{blue}[c]	⋯	4	4
f_{blue}[c]	⋯	13%	6%
N_{mult}[d]	129	13	29
f_{mult}[d]	41%	41%	45%
$N_{mult,blue}$[e]	33	3	6
$f_{mult,blue}$[e]	10%	9%	9%
$\langle \lvert\Delta v_{peaks}\rvert \rangle$ (km s^{-1})	615 ± 14	608 ± 49	716 ± 35
$\langle F_{H\alpha} \rangle$ (10^{-17} cgs)	⋯	1.3 ± 0.1	7.2 ± 0.7
$\langle \sigma_{neb} \rangle$ (km s^{-1})	⋯	34 ± 4	84 ± 4

Notes.
[a] Parameters for the subset of LAEs with MOSFIRE nebular (systemic) redshifts.
[b] Averages are given as mean values, with uncertainties denoting the standard error of the mean.
[c] Number (or fraction) of objects with a blueshifted Lyα line ($v_{Ly\alpha,peak} < 0$).
[d] Number (or fraction) of objects with multiple detected Lyα peaks.
[e] Number (or fraction) with multiple detected Lyα peaks that have a lower-velocity ("blue") dominant peak.

In this case, the blueshifted Lyα emission could conceivably correspond to outflowing gas illuminated externally by the nearby QSO, a situation that could explain the association of blue-dominant LAEs with the background of the QSO, where the geometry would naturally predict blueshifted emission from

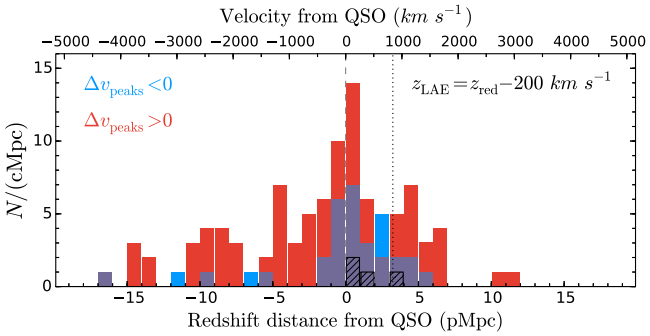

Figure 10. Redshift distribution of multi-peaked Lyα lines with respect to their corresponding HLQSOs. Color-coding of the stacked histogram matches Figure 9 (top panel) and Figure 11. The dashed gray line corresponds to LAEs at the HLQSO redshift. The dotted black line corresponds a distance 10 Mlyr behind the HLQSO, the upper bound on the region that could emit detectable QSO-generated fluorescent emission for a 20 Myr QSO lifetime (as argued in Trainor & Steidel 2013). Here, the LAE systemic redshifts are assumed to be -200 km s^{-1} from the *red* Lyα peak. Under this assumption, the blue-peaked LAEs are highly biased toward the rear of the nearby QSOs. Black hatched bars denote the *systemic* redshifts measured for the 4 LAEs with blueshifted Lyα peaks ($v_{Ly\alpha,peak} < 0$ km s^{-1}), which appear to occupy a similar physical volume as the blue-dominant multipeaked LAEs.

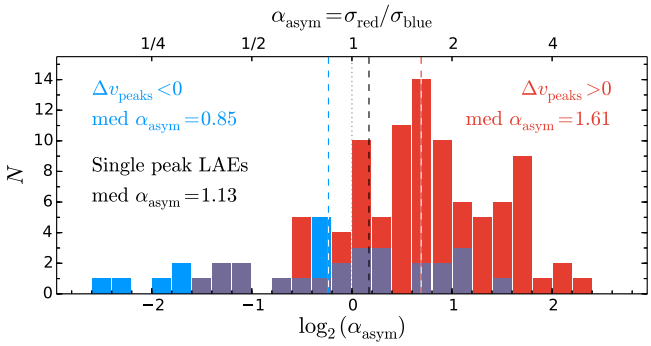

Figure 11. Lyα line asymmetries for LAEs with multi-peaked Lyα detections. The reported asymmetry corresponds to the primary peak of the multi-peaked line. Red bars give the asymmetry distribution of red-peak-dominant systems ($\Delta v_{peaks} > 0$), while blue bars correspond to blue-peak-dominant systems ($\Delta v_{peaks} < 0$) according to the top panel of Figure 9. The blue-white dashed line is the median asymmetry of the $\Delta v_{peaks} < 0$ sample and the red-white dashed line is that of the $\Delta v_{peaks} > 0$ sample. For comparison, the black dashed line gives the median asymmetry of the sample of spectral Lyα lines without multiple detected peaks.

the QSO-facing side of a gaseous outflow. Only three of the blue-dominant LAEs currently have MOSFIRE spectra, but their systemic redshifts place them 0.4–1.2 pMpc in the background of the QSO (consistent with the Lyα-only measurements). Similarly, the 4 LAEs with MOSFIRE redshifts and $v_{Ly\alpha,peak} < 0$ km s^{-1} (that is, objects with blueshifted Lyα with respect to systemic) lie in the immediate background of the QSO (0.4–4 pMpc; hatched region in Figure 10), suggesting that external illumination may play a role in their spectral morphology as well.

Detailed predictions for fluorescent emission from gas with large bulk velocities and a realistic spatial distribution are unclear (although see work by Kollmeier et al. 2010), and it is difficult to draw robust conclusions without access to the systemic redshifts of these LAEs. Given the diversity of line morphologies and asymmetries even within the set of blue-dominant LAEs (Figure 8), it is unclear whether these atypical profiles are generated by a single mechanism. Further study of these "blue" LAEs, including additional rest-frame optical spectroscopy, is required to understand the physics of their Lyα emission and transmission.

Finally, in the absence of systemic redshift measurements and/or multiple emission peaks, the Lyα line asymmetry (α_{asym}; Section 2.2) may also trace gas kinematics among these LAEs (see, e.g., Zheng & Wallace 2014). However, line asymmetry is often not evident in medium-resolution, low-S/N spectra. Not only will the measured line asymmetry be systematically diminished by the smoothing effect of the convolved line spread function, but noise peaks and unresolved emission line features may be fit by an extended tail by our automatic fitting algorithm.

Despite these issues, some trends can be seen in the relative distributions of Lyα line asymmetries. Figure 11 shows the distribution of α_{asym} for blue-dominant and red-dominant multi-peaked LAEs. While both subsamples have broad distributions of α_{asym} because of the effects described above, there is a clear tendency of the blue-dominant Lyα lines to have lower values of α_{asym} (that is, an extended blue wing in the primary peak), while red-dominant LAEs typically have $\alpha_{asym} > 1$ (extended red wings). The two distributions have a Kolmogorov–Smirnov probability of being drawn from the same underlying distribution $p < 4 \times 10^{-5}$. This result agrees with the findings of Yamada et al. (2012a), who found a similar relation (albeit with lower significance) in their smaller sample.

3.4. LBG Lyα Line Morphologies

We compare the distribution of Lyα morphologies between the KBSS-Lyα LAEs and the KBSS LBGs in Figures 12 and 13, as well as in Table 3. In the LBG sample, 29/65 (45%) have a detected secondary peak. Of these objects, 23/29 (79%) are red-peak dominant. Note that these rates are 40% and 74%, respectively, among the LAEs (Table 6). As described above, measured rates of Lyα peak multiplicity are dependent on both the resolution and S/N of the spectra. The KBSS LBGs considered in this paper were observed using the same instrument setup as the KBSS-Lyα LAEs and were analyzed using the same line-detection software (see Section 2.2); however, the typical LBG Lyα fluxes are significantly brighter (Table 6) and the spectral S/N is correspondingly higher. Secondary peaks of low relative significance are therefore more likely to be detected in the LBG sample than in our LAE sample. In particular, we find that the ratio of primary-peak flux to secondary-peak flux is larger among the LBGs than the LAEs, which may be caused by missing similarly faint secondary Lyα peaks in the LAE spectra. However, radiative transfer models of Lyα escape also predict that the primary/secondary flux ratio increases with outflow velocity (e.g., Verhamme et al. 2006). In either case, the frequency of Lyα peak multiplicity and blue-dominant Lyα peaks are broadly consistent between our LBG and LAE samples.

However, the velocity distribution of Lyα flux varies significantly between the LAE and LBG samples. Figure 12 displays the distribution of fit Lyα emission line widths for both samples of objects. The measured line width is that of the primary Lyα peak, and is given by the average of the red and blue scale parameters of the asymmetric Gaussian fit

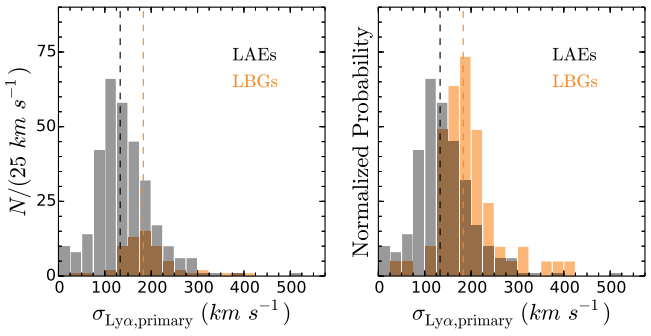

Figure 12. Distribution of fit widths (Equation (5)) for the primary Lyα peak among the 318 KBSS-Lyα LAEs (gray) and the 65 LBGs in the KBSS LBG (orange) sample lines. The LRIS instrumental resolution of $\sigma_{\mathrm{inst}} = 100$ km s^{-1} has been subtracted in quadrature; fit widths less than 100 km s^{-1} are plotted as zero. The left panel shows the number distribution of object line widths, while the right panel presents the same data normalized as a probability distribution for ease of comparison. The median width for each sample is marked with a dashed line.

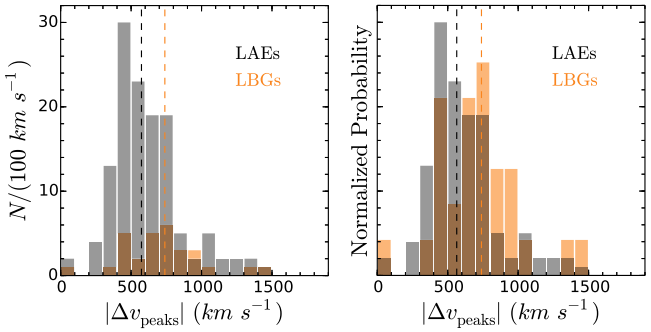

Figure 13. Distribution of Lyα peak separations among the 129 LAEs in Figure 9 (gray) and the 29 LBGs in the KBSS LBG (orange) sample with multi-peaked Lyα emission lines. Given the smaller size of the LBG sample, positive and negative separations of the same size are grouped together (unlike Figure 9). The left panel shows the number distribution of of objects, while the right panel presents the same data normalized as a probability distribution for ease of comparison. The median separation for each sample is marked with a dashed line.

(Equation (2)):

$$\sigma_{\mathrm{Ly}\alpha,\mathrm{primary}} = \frac{\sigma_{\mathrm{red}} + \sigma_{\mathrm{blue}}}{2}. \quad (5)$$

The LAE sample has a median line width of 166 km s^{-1}, with 33% of spectra having a primary-peak line width less than 150 km s^{-1}. The LBG sample has a median line width of 210 km s^{-1}, with only 3% (two spectra) having a primary-peak line width less than 150 km s^{-1}. The LRIS spectral resolution $\sigma_{\mathrm{inst}} = 100$ km s^{-1} (which is the same for both the LAE and LBG samples) has been subtracted in quadrature. Note that nearly all the measured lines are well-resolved with respect to the resolution limit. A Kolmogorov–Smirnov test gives a probability $p \approx 10^{-10}$ of both samples being drawn from the same distribution.

A similar contrast is seen in the distribution of peak separations among the LAEs and LBGs with multiple detected emission peaks (Figure 13). Among the 129 LAEs with multiple detected peaks, the median peak separation is $\langle|\Delta v_{\mathrm{peaks}}|\rangle = 565$ km s^{-1}, while the 29 LBGs with multiple peaks have $\langle|\Delta v_{\mathrm{peaks}}|\rangle = 780$ km s^{-1}. Note that unlike Figure 9, only the absolute value of the separation is considered here. A Kolmogorov–Smirnov test gives a probability $p \approx 10^{-3}$ of both samples being drawn from the same distribution. As above, the finite resolution of our spectra censors the distribution of peaks with small separations, but the typical separations observed exceed our resolution limit by a large factor, suggesting that we are able to resolve the intrinsic distribution of peak separations for each sample. Furthermore, our use of the same instrument setup and line-analysis algorithms for both the LAE and LBG samples allows us to demonstrate an instrinsic difference between the two populations.

In contrast to the results of Yamada et al. (2012a), we find no significant correlation between the Lyα peak width and peak separation among multi-peaked profiles for our LAE sample, and only a moderate association among the LBGs (Pearson correlation $r \approx 0.3$, $p \approx 0.05$). However, these parameters are highly correlated (although with significant scatter) in the combined LBG+LAE sample, for which a Pearson correlation test yields $p \approx 10^{-4}$ ($r \approx 0.3$).

Here we have defined the peak separation by the velocity difference between the peaks of the two most dominant components of the Lyα emission line, rather than the flux-weighted centroids of those components. Because the typical Lyα emission lines have redshifted primary peaks with asymmetric extended red tails (particularly for the LBGs; Figure 6), using flux centroids or symmetric Gaussian fits to define the peak separation would lead to (1) a larger median peak separation for both samples, and (2) a larger difference between the LAE and LBG distributions.

For comparison, the distribution of nebular line widths for both the LAEs and LBGs is given in Figure 14. As discussed in Section 3.2, the nebular line widths trace the velocity dispersion of the stars and H II regions within the galaxy. The larger nebular line widths of LBGs with respect to LAEs are therefore likely to reflect the larger masses of continuum-bright galaxies with respect to faint LAEs. Further discussion of the mass-dependence of the interstellar and circumgalactic properties of these galaxies is reserved for Section 5.

In contrast, the velocity distribution of emergent Lyα flux depends most sensitively on the velocity distribution and the optical depth of the scattering H I gas. The observed spectral morphologies therefore suggest that LBGs are associated with higher velocity and/or more optically thick outflows than their LAE analogs. It is thus evident that the observational characteristics that govern a galaxy's selection by the narrowband-excess and/or continuum-color techniques (namely, the observed Lyα and continuum emission) must be linked to properties of the outflowing gas—whether directly (by the coupling of Lyα photons to interstellar and circumgalactic gas) or indirectly (through the star-forming regions that produce Lyα, far-UV, and ionizing photons and presumably provide the energy/momentum for large-scale galactic outflows). In the remainder of this paper, we separate these effects of gas velocity and optical depth on the emitted spectrum by considering the absorption and emission profiles in composite galaxy spectra.

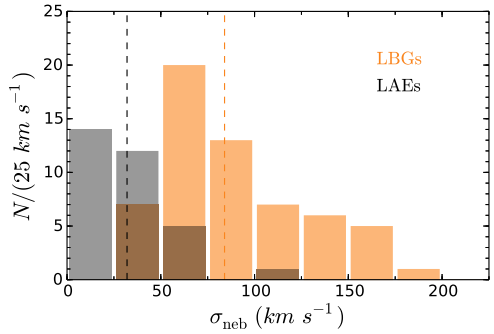

Figure 14. Distribution of nebular line widths for LAEs (gray) and KBSS LBGs (orange) for the subset of objects with MOSFIRE rest-optical spectra. Dashed lines denote the average line width for each sample. The instrumental resolution of 35 km s^{-1} has been removed from each value; objects consistent with this resolution have been assigned $\sigma_{\rm neb} = 0$. A typical LBG has a nebular line width $\sim$2$\times$ that of a typical LAE.

4. SIGNATURES OF OUTFLOWS IN STACKED SPECTRA

4.1. Absorption Signatures of Outflows

While the resonance of the Lyα transition makes it a sensitive tracer of gas in and around high-redshift galaxies, this strong coupling can obscure the details of the physical processes driving Lyα absorption and emission. In particular, we noted in Section 3 that Lyα transmission is sensitive to a variety of factors, including the optical depth, covering fraction, dust content, and kinematics of the gas distribution. Because they produce degenerate effects on the Lyα profile, Lyα emission alone is insufficient to fully characterize the physical conditions among LAEs or high-redshift galaxies generally.

The measurement of absorption lines in the rest-UV continuum spectra of galaxies is thus a crucial tool for disentangling these effects. Kunth et al. (1998) analyzed the spectra of nearby Lyα-emitting galaxies, finding blueshifted metal absorption features from enriched, outflowing gas. This study noted the correspondence of the Lyα emission and metal absorption in tracing the velocity structure and porosity of the interstellar gas. At higher redshifts, the analysis of the continuum spectra of typical star-forming galaxies began with spectra of the gravitationally lensed $z \sim 2.7$ galaxy MS 1512-cB58 (Pettini et al. 2000, 2002) and was extended to non-lensed galaxies through stacking the spectra of many ($\sim$1000) $z \sim 3$ LBGs by Shapley et al. (2003). These studies utilized the high S/N of the lensed or stacked spectra to extract metal abundances, ion-specific covering fractions, outflow velocities, and systemic redshifts for the galaxies while placing these properties in the context of their SFRs, masses, and Lyα emission properties. Steidel et al. (2010) presented both interstellar absorption line features and Lyα emission in the context of a unified kinematic model for gas outflows in LBGs (Section 5 of that paper). For faint LAEs such as those in our sample, constraints on the metal content and outflow velocities are especially interesting because they reveal the extent to which past and ongoing star formation are already having an effect on the chemistry and kinematics of these particularly young, low-mass galaxies.

LAEs are by selection generally faint in the continuum, so absorption measurements of comparable fidelity to those of Shapley et al. (2003) present a significant challenge, particularly for objects as faint as those considered here. Hashimoto et al. (2013) studied the absorption profiles in a stack of four LAEs with systemic redshift measurements to measure outflow velocities, and Shibuya et al. (2014) conducted a similar analysis for four individual bright LAEs, finding typical outflow velocities $v_{\rm abs} \sim$ 100–200 km s^{-1}. As noted in Section 1, however, the objects in these studies have B-band magnitudes $\langle m_{\rm B}\rangle \sim 24$ ($L \sim L_*$), meaning that they easily fall within typical selection criteria for continuum-selected star-forming galaxies. While useful for studying the correlation between outflow velocity $v_{\rm abs}$ and $W_{{\rm Ly}\alpha}$, these samples are clearly far removed from the faint LAEs considered in this paper, with median continuum magnitude $\langle m_{\rm B}\rangle = 26.8$ ($L \sim 0.1L_*$, $\sim$10$\times$ fainter than these previous samples).

For such faint objects, large samples are needed to obtain even a low-fidelity measurement of metal absorption. To make such a measurement, we stack the rest-UV spectra of all 318 spectroscopic KBSS-Lyα LAEs using a rest frame defined by $z_{{\rm sys,Ly}\alpha} = z_{{\rm Ly}\alpha,{\rm peak}} - 200$ km s^{-1} based on the redshift calibration of Section 3.2. As many of our objects have multiple LRIS spectra of their rest-UV continuum, we include all spectra for each object such that each spectrum receives equal weighting, effectively weighting each object by total exposure time.[12] Furthermore, two spectra with individually significant continua (possibly AGN) were removed from the sample in order to ensure that they did not dominate the stack; all the remaining spectra have S/N $\ll 1$ per pixel in the continuum individually. Finally, the portion of each spectrum corresponding to $\lambda \approx 5577 \pm 15$Å in the observed frame was omitted from the stack in order to remove contamination from a bright sky line. In total, 422 LAE spectra were stacked, producing a final spectrum with an effective exposure time of $\sim$675 hr (all from the Keck I 10 m telescope).

An error spectrum was then generated for the stack via a bootstrapping procedure. 1000 iterations were performed in which 422 spectra were drawn (with replacement) from our sample and stacked to make a set of 1000 randomized spectral stacks. The standard deviation of values at each pixel was then used to define the error spectrum of the true stacked data.[13] From this error spectrum, we estimate that the stack has a median S/N $\sim$10 per pixel in the range 1230 Å$\lesssim \lambda_{\rm rest} \lesssim$ 1420 Å, the range of interest for the absorption lines discussed below.[14]

Measurements were made of the absorption of six metal lines, corresponding to four spectral regions (Figure 15, Table 4). For each spectral region, the continuum level was independently estimated using the local median value, but the continuum estimates among all four regions are consistent to $\lesssim$2% in λf_λ units. The measured continuum was also checked for consistency with the broadband photometry. At the median wavelength of the absorption lines ($\lambda_{\rm obs} \sim 5000$ Å), the stacked continuum flux density is

[12] The results of the continuum stacking are insensitive to whether the objects are weighted equally, weighted by number of spectra, or weighted by total exposure time.

[13] The error spectrum thus includes the variance in continuum level at each pixel, so it is a conservative estimate of the error in the mean spectrum.

[14] Unfortunately, we are unable to obtain robust measurements of the C IV doublet 1549,1551 Å, generally one of the strongest absorption lines in high-redshift galaxies and a key indicator of AGN activity when seen in emission. Because we favor the resolution of the 600-line grism over the increased spectral range of the 300 or 400-line grisms, the C IV doublet falls off the spectrograph for many of our objects. Furthermore, the particular redshift range of our LAEs ($z \sim 2.6$) causes significant contamination near $\lambda_{\rm rest} \sim 1550$ Å due to the bright sky line at $\lambda_{\rm obs} \sim 5577$ Å.

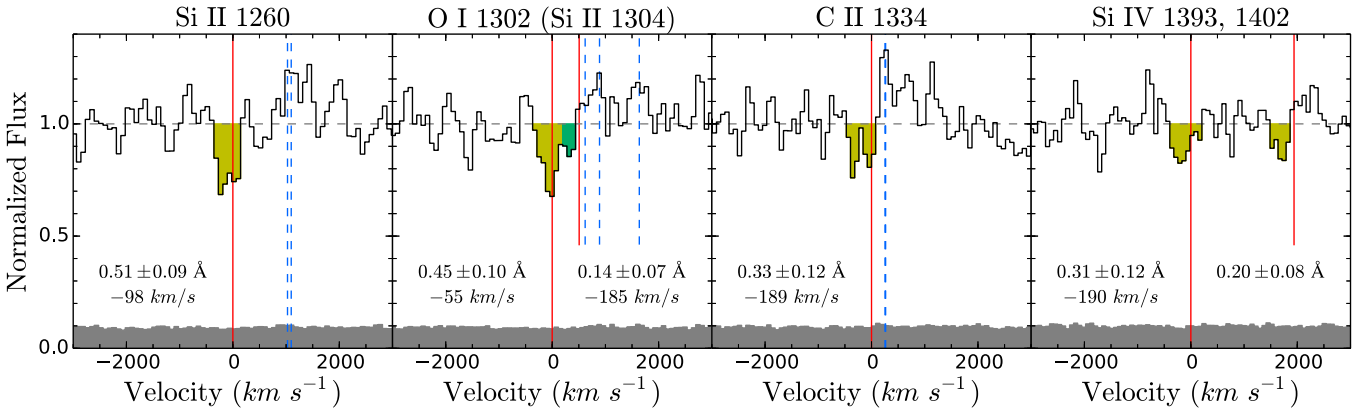

Figure 15. Interstellar absorption signatures of metal lines in the stacked spectrum of all 318 spectroscopic LAEs. Vertical red lines are the rest-wavelengths of metal ions seen in absorption, while dashed blue lines denote the wavelengths of fine-structure and nebular emission features. A detailed list of these lines is given in Table 4. Yellow shaded regions are the areas used to calculate the equivalent width and absorption-weighted velocity of each species; the absorption estimated for Si II λ1304 is shaded green to differentiate it from the partially blended O I λ1302 absorption. Uncertainties for the equivalent width measurements are estimated via a bootstrapping procedure described in the text, and the bootstrapped error spectrum is displayed in gray at the bottom of each panel.

7.5×10^{-8} Jy ($m_{5000} = 26.72$), comparable to the mean Lyα-subtracted broadband B/G flux (7.9×10^{-8} Jy; $\langle m_{\rm BB} \rangle = 26.66$) measured photometrically among the 318 objects in the spectral stack. Absorption measurements were then made for the low-ionization lines Si II λ1260, O I λ1302, Si II λ1304, and C II λ1334, as well as the higher-ionization doublet Si IV $\lambda\lambda$ 1393,1402. The equivalent width of absorption is estimated in each case by numerically integrating the set of contiguous pixels with $f_{\rm norm} < 1$ nearest the rest-frame metal-line wavelength in the normalized stack. The O I λ1302 and Si II λ1304 absorption lines are partially blended, so the division between them was determined by visual inspection of the stacked spectrum. This division was cross-checked in bootstrapped composite spectra resampled at a range of wavelength scales. Uncertainties in the equivalent widths were computed by performing the same measurement for each line in each of the 1000 bootstrap spectra; the quoted error refers to the standard deviation of these bootstrap measurements. An absorption-weighted velocity was then measured for each line via numerical integration of the line profile: $v_{\rm abs} = \int_{\Delta v} [1 - f_{\rm norm}(v)]\, v dv / \Delta v$. While the equivalent widths in absorption of the two lines in the Si IV doublet were measured separately, they were constrained to have the same total absorption-weighted velocity.

All the measured absorption lines have mean velocities $-100 \lesssim \langle v_{\rm abs} \rangle \lesssim -200$ km s^{-1} with absorption extending to $v_{\rm abs} \sim -500$ km s^{-1} (where negative velocities indicate blue-shifted absorption), in good agreement with the brighter LAE samples of Hashimoto et al. (2013) and Shibuya et al. (2014). We therefore find clear evidence for blueshifted metal absorption signatures in these $L \sim 0.1L^*$ LAEs, a strong indicator of the presence of metal-enriched outflowing gas.

Because the systemic redshifts are not precisely known for the LAEs in our stack, there may be some additional uncertainty in our measured velocities compared to those measured in samples with complete catalogs of systemic redshifts. However, our stacked spectra also show several fine-structure and nebular emission features (dashed vertical lines in Figure 15) that are more likely to trace the systemic galaxy redshifts; the correspondence of these peaks to the rest-frame wavelengths of these features further suggests that our corrected Lyα line measurements are a good proxy for the redshifts in these LAEs. Notably, we have not corrected the line strengths or velocities for emission from nearby fine-structure transitions; the effects of this contamination likely causes an underestimate of intrinsic absorption and overestimate of the velocity of Si II λ1304 and C II λ1334.

Galaxy outflows may also be characterized by the covering fraction of the UV continuum by absorbing materials and its optical depth. While these properties are typically degenerate for individual transitions (except at much higher S/N and resolution), they may be constrained independently when

Table 4
LAE Continuum Absorption Features

Ion	$\lambda_{\rm lab}$[a] (Å)	$f_{\rm osc}$[b]	$W_{\rm ion}$[c] (Å)	A_{ki}[d] (10^8s^{-1})
Absorption Features				
Si II[e]	1190.416	0.575	0.53 ± 0.15	···
Si II[e]	1193.290	0.277	0.24 ± 0.11	···
Si II	1260.422	1.22	0.53 ± 0.10	···
O I	1302.169	0.0520	0.43 ± 0.10[f]	···
Si II	1304.370	0.0928	0.17 ± 0.08[f]	···
C II	1334.532	0.129	0.32 ± 0.11	···
Si IV	1393.760	0.513	0.30 ± 0.12	···
Si IV	1402.773	0.255	0.21 ± 0.08	···
Emission Features				
Si II*	1264.738	···	···	30.4
Si II*	1265.002	···	···	4.73
O I*	1304.858	···	···	2.03
O I*	1306.029	···	···	0.676
Si II*	1309.276	···	···	6.23
C II*	1335.663	···	···	0.476
C II*	1335.708	···	···	2.88

Notes.
[a] Vacuum wavelength of transition.
[b] Oscillator strength from the NIST Atomic Spectra Database (www.nist.gov/pml/data/asd.cfm).
[c] Equivalent width of absorption in stacked LAE spectrum (Figure 15).
[d] Einstein A-coefficients from the NIST Atomic Spectra Database.
[e] The Si II $\lambda\lambda$1190,1193 doublet is in the continuum blueward of Lyα, which suffers from lower S/N and a high density of absorption and emission lines. As such, these features are only used here to constrain the saturation of Si II λ1260.
[f] The O I λ1302 and Si II λ1304 absorption lines are partially blended, so the division between them is somewhat uncertain.

multiple transitions of the same species are present. In particular, the expected ratio of the equivalent widths of Si II λ1304 and Si II λ1260 is $W_{1260}/W_{1304} = 12.3$ when both transitions are optically thin. The measured ratio of these lines in the LAE composite spectrum is $W_{1260}/W_{1304} = 3.6$, consistent with a saturated Si II λ1260 transition, with the caveat that the measured Si II λ1304 absorption has small S/N and is partially blended with the O I λ1302 line. To clarify this measurement, we consider the absorption due to the Si II $\lambda\lambda$ 1190,1193 doublet in the rest-EUV ($\lambda_{\rm rest} \lesssim 1200$ Å) spectrum. The high density of absorption and emission lines and lower continuum level of the spectrum shortward of Lyα (including foreground Lyα absorption) result in larger uncertainties in these line strengths, but both lines of the doublet are detected with high significance.

The measured absorption equivalent widths (W) for each of the four Si II transitions are given in Table 4, along with the corresponding vacuum wavelengths (λ) and oscillator strengths ($f_{\rm osc}$). In the optically thin regime, these quantities are related to the column density of absorbing material by $N_{\rm ion} \propto W_i/\lambda_i^2 f_{{\rm osc},i}$ for each transition of index i. Because the physical column density of a single ionic species must be single-valued, the quantity $W/\lambda^2 f_{\rm osc}$ will likewise be constant for all ground-state transitions of the same ion unless one or more transitions have saturated. In this latter case, $W/\lambda^2 f_{\rm osc}$ will decrease with increasing $f_{\rm osc}$.

The quantity $W/\lambda^2 f_{\rm osc}$ is compared for the four Si II transitions in Figure 16. The Si II λ1190, λ1193, and λ1304 transitions are consistent with a single value of $W/\lambda^2 f_{\rm osc}$, but the Si II λ1260 absorption falls significantly below the weighted average of the other three lines, indicating saturation. While the other three transitions appear to be optically thin, both Si II λ1193 and Si II λ1304 have nearby excited fine-structure emission transitions that may bias our measurements toward lower equivalent widths, as discussed above. If the Si II λ1304 line were saturated, however, the bottom of its absorption trough would reach a similar depth as the saturated Si II λ1260 transition with respect to the local continuum (as is seen in some LBG samples; see Section 4.3), which is clearly not the case in the LAE composite spectrum (Figure 15). This suggests that any filling-in of the absorption by excited fine-structure emission has a small effect on the total measured absorption. The analysis of the composite spectrum thus strongly suggests that $\tau_{1260} > 1$, $\tau_{1304} \ll 1$, and $\tau_{1190} \sim \tau_{1193} \lesssim 1$ based on the consistency of the curve-of-growth analysis in Figure 16 (where τ_λ is the central optical depth of the Si II transition at wavelength λ).

Given the saturation of Si II λ1260, the maximum depth of the line profile with respect to the continuum indicates a covering fraction of Si II-enriched outflowing gas $f_c \approx 0.3$ among the LAEs. While multiple unambiguous absorption features are not available for other low-ionization species in the composite, the consistency of the absorption profile depths and widths for the O I λ1302 and C II λ1334 with the saturated Si II λ1260 line suggests that those species are co-spatial with Si II and have a similar covering fraction. We therefore take the covering fraction of low-ionization gas outflows to be $f_c \approx 0.3$ for the LAE sample, noting the possible existence of narrow absorption components unresolved by our $R \sim 1300$ spectra.

The two lines of the Si IV doublet have a measured ratio $W_{1393}/W_{1402} = 1.4$, suggesting that the doublet is also saturated ($W_{1393}/W_{1402} = 2$ on the linear part of the curve of growth).

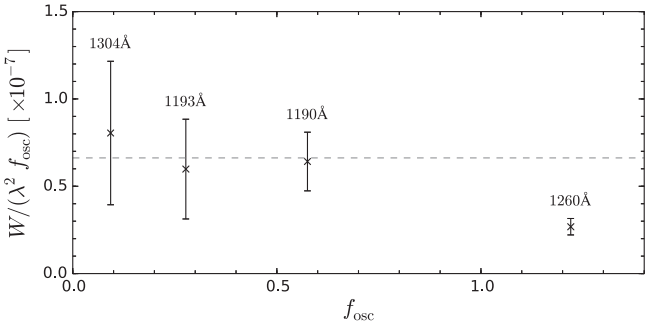

Figure 16. Curve-of-growth analysis for the 4 detected Si II lines in the stacked LAE spectrum. The scaled equivalent width of absorption for each transition i is given by $W_i/\lambda_i^2 f_{{\rm osc},i}$, which is proportional to the column density of the ion (and thus equal for all transitions) if the transition is unsaturated. If transitions are saturated, $W_i/\lambda_i^2 f_{{\rm osc},i}$ will decrease with increasing $f_{{\rm osc},i}$. Errorbars are the 1σ uncertainties on W_i from the bootstrap analysis. The dashed horizontal line is the best-fit constant value of $W/\lambda^2 f_{\rm osc}$ for the three transitions with the lowest values of $f_{\rm osc}$ (the least likely to be saturated).

However, the weaker line has S/N ~ 2, and $\sim$25% of the bootstrap spectra have $W_{1393}/W_{1402} \gtrsim 2$, so the transition may in fact be optically thin. The higher ionization potential of Si IV (33.5 eV) requires radiation from hot stars and/or collisional ionization in $T \gtrsim 10^4$ K gas, and therefore traces more strongly ionized gas in or around the galaxy. The depth of the two absorption lines thus suggests the presence of an ionized medium with an average covering fraction $f_c \sim 20\%$ (or greater if the lines are optically thin). It is unclear whether this gas is co-spatial with the medium giving rise to the lower-ionization lines described previously; this relationship is probed further by comparing the velocity profiles of their absorption below.

It is important to note that all of the above constraints on the covering fraction of metal-enriched gas rely on the assumption that the metal-line photons scattered out of the galaxy spectrum are emitted away from our line of sight to the galaxy. In the limit that the scattering medium is entirely co-spatial with the observed light distribution from the galaxy (and that the scattering is isotropic and photon-conserving), we would expect that the net emission and absorption from scattering would be zero. In reality, many photons will be scattered at large radii with respect to the light profile of the galaxy, particularly for transitions where excited fine-structure states provide an alternative escape pathway with low optical depth. Given the spatial compactness of the LAEs, however, this "emission-filling" may reduce the observed absorption, particularly for those transitions without nearby excited fine-structure states such as Si IV $\lambda\lambda$1393,1402. This effect may partially explain the lower measured value of f_c for the Si IV transitions, in addition to their unknown optical depth.

The velocity shift of Lyα emission shows a strong inverse trend with Lyα equivalent width in the collective populations of high-redshift LAEs and LBGs (Erb et al. 2014), but there are many mechanisms that could underly this relationship. If a change in outflow velocity is the driver, then we should expect the velocity profile of the metal absorption lines tracing the outflows to vary with $W_{{\rm Ly}\alpha}$ as well. Unfortunately, the S/N in stacked subsamples is too low to probe this effect in individual lines. However, we can boost the S/N by combining the line profiles for multiple lines that we expect to trace the same gas. In particular, we can stack the low-ionization lines (corresponding to more neutral H I gas) and the high-ionization lines

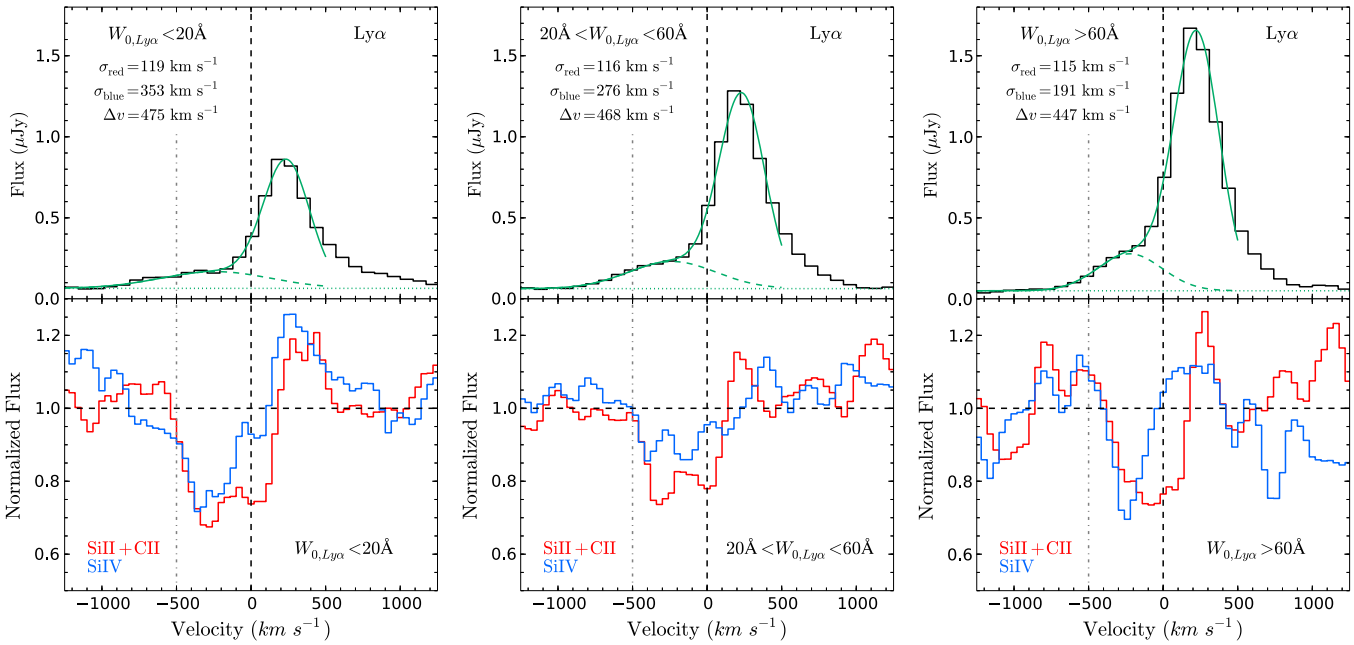

Figure 17. Lyα emission and interstellar absorption signatures in stacked subsets of spectra grouped by their photometric Lyα equivalent width, $W_{Ly\alpha}$. Details of each subsample are given in Table 5. Top panels: Lyα emission spectra (black), and profile fit (green) for each subsample. The solid green line is the full fit, the dotted green line is the fit continuum level, and the dashed green line is the blueshifted Gaussian component of the fit. The fits do not extend to $v > +500$ km s^{-1}, as this portion of the spectrum was omitted during fitting. Dashed and dotted–dashed vertical lines denote $v = 0$ and $v = -500$ km s^{-1}, respectively. Note that the specific flux in μJy is measured in the observed frame. Bottom panels: red curves are the average absorption profiles of the low-ionization species Si II λ1260 and C II λ1334, while blue curves are the absorption profiles of the more highly ionized Si IV (λ1393 and λ1402). O I λ1302 and Si II λ1304 are omitted due to blending. As above, dashed and dotted–dashed vertical lines denote $v = 0$ and $v = -500$ km s^{-1}, while the dashed horizontal line denotes the local continuum level.

(corresponding to more highly ionized H II gas) and thereby extract enough signal to compare the variation of the gas velocity distribution with $W_{Ly\alpha}$.

Spectra combined in this way are displayed in Figure 17 for three subsamples divided according to $W_{Ly\alpha}$, with median $W_{Ly\alpha} \approx 11$, 37, and 110 Å respectively. Because these stacks include features at multiple wavelengths, we subsampled them by a factor of two with respect to the original wavelength scale before stacking in order to maximize the velocity resolution of the stacks. Details of these subsamples are in Table 5.

Several key features are apparent in the bottom panels of Figure 17. First, there is substantial absorption by low-ionization species in all three panels at the systemic redshift of the galaxy ($v = 0$), but there is little or no corresponding high-ionization absorption. At the negative edge of the absorption profiles ($v \sim -500$ km s^{-1}), however, the high-ionization and low-ionization absorption are well aligned in each panel. This pattern may indicate that both ionized and neutral gas are present in the material most likely associated with an outflow, but that the interstellar medium is dominated by neutral H I and low-ionization metals at $v = 0$. As noted above, however, the Si IV transition is particularly sensitive to emission-filling, which will tend to systematically reduce the observed absorption at $v \approx 0$.

Second, if the absorption lines are assumed to be optically thick, there is a slight variation in covering fraction as a function of $W_{Ly\alpha}$: $f_c \sim 30\%$ for the $W_{Ly\alpha} \sim 11$ Å sample, $f_c \sim 20\%$ for the intermediate sample, and $f_c \sim 25\%$ for the highest-$W_{Ly\alpha}$ sample. The decline in f_c from $W_{Ly\alpha} \sim 11$ Å to $W_{Ly\alpha} \sim 37$ Å is consistent with expectations for Lyα-emitting galaxies: Steidel et al. (2010) demonstrate that observed Lyα-emission is closely correlated with the covering fraction of the gas through which these photons escape. The increase in apparent f_c between the $\langle W_{Ly\alpha} \rangle = 37$ Å and $\langle W_{Ly\alpha} \rangle = 110$ Å samples may not be significant because the continuum emission is extremely faint in the latter stack; not only is the statistical error large, but small systematics in the spectroscopic background subtraction could be significant in the stack of these faint objects, possibly biasing the measured continuum level. However, the consistency between the photometric and spectroscopic continuum estimates suggests this effect should be quite small. In any case, it seems that the apparent depth of the interstellar absorption features correlates only weakly with $W_{Ly\alpha}$ for the faintest, highest-$W_{Ly\alpha}$ bin of galaxies.

Third, there is some dependence in the maximum absorption velocity as a function of $W_{Ly\alpha}$. While the absorption extends to $v_{abs} \sim -500$ km s^{-1} in all three panels, the $W_{Ly\alpha} \sim 11$ Å stack shows absorption in Si IV extending to higher velocities at low optical depths. Conversely, the most-blueshifted edge of absorption in the $W_{Ly\alpha} \sim 110$ Å stack extends no further than $v_{abs} \sim -400$ km s^{-1}.[15] It is important to note that the systematic velocities used here are derived from a constant correction to the Lyα redshift, and thus the evolution of the Lyα offset with $W_{Ly\alpha}$ could theoretically mimic an evolution in absorption velocity with $W_{Ly\alpha}$. However, despite previous measurements of the significantly smaller Lyα offsets among LAEs with respect to LBGs, we find that the *peak* of the Lyα profile has a consistent 200 km s^{-1} redshift with respect to systemic at our observed resolution for both LBGs and LAEs (Section 3.2). Furthermore, no difference with $W_{Ly\alpha}$ is observed in the most-redshifted edge of the low-ionization absorption (presumably corresponding to neutral interstellar gas at the systemic

[15] Note that the maximum absorption velocity is insensitive to any bias in the continuum level due to systematics in the background subtraction.

Table 5
Lyα Spectroscopic Subsamples and Composite Lyα Emission Profiles

Subsample	$\langle W_{Ly\alpha}\rangle$	$\langle\mathcal{R}\rangle$	N_{obj}	N_{spec}[a]	σ_{red} (km s^{-1})[b]	σ_{blue} (km s^{-1})[b]	Δv (km s^{-1})[b]
Lyα Redshifts[c]							
$W_{Ly\alpha} \geqslant 60$ Å	110Å	27.6	158	211	115 ± 5	191 ± 10	447 ± 7
$20 \leqslant W_{Ly\alpha} < 60$ Å	37Å	26.8	160	211	116 ± 5	276 ± 15	468 ± 7
$W_{Ly\alpha} < 20$ Å[d]	11Å	26.6	82	94	119 ± 7	353 ± 37	475 ± 10
KBSS LBGs	27Å	24.4	65	65	178 ± 10	226 ± 8	646 ± 20
Systemic Redshifts							
MOSFIRE LAEs	44Å	26.9	32	57	131 ± 9	234 ± 14	490 ± 23
KBSS LBGs	27Å	24.4	65	65	215 ± 20	246 ± 11	568 ± 25

Notes.
[a] Because some objects were observed multiple times, and all available spectra were combined in each continuum stack, $N_{spec} > N_{obj}$.
[b] The parameters σ_{red}, σ_{blue}, and Δv are the velocity widths of the red peak, blue peak, and peak separation in the fit to the composite Lyα spectrum (Figures 17 and 18). The peak widths reflect the subtraction in quadrature of the LRIS instrumental resolution of $\sigma_{inst} = 100$ km s^{-1}.
[c] Composite spectra constructed using Lyα redshifts, shifted by -200 km s^{-1}.
[d] Objects observed on the basis of a narrowband excess and spectroscopically detected Lyα emission line, but which have $W_{Ly\alpha}$ smaller than the adopted threshold of $W_{Ly\alpha} \leqslant 20$ Å.

redshift) across the three panels of Figure 17; such a shift would be expected from a $W_{Ly\alpha}$-dependent estimator of the systemic redshift. Lastly, the total velocity width of absorption decreases significantly with increasing $W_{Ly\alpha}$ across the three panels, suggesting the presence of a real anti-correlation of Lyα equivalent width with outflow velocity among these faint LAEs.

Given that $W_{Ly\alpha}$ is likely to be anti-correlated with SFR and stellar mass among these LAEs (as discussed in Section 3.1), we interpret the above trends as a positive correlation between SFR and outflow velocity. A similar analysis of the KBSS LBG sample (Figure 18, discussed further in Section 4.3) suggests a continuation of this trend to higher SFRs.

4.2. Lyα Emission Signatures of Outflows

The composite Lyα emission profiles for each subsample (top panels of Figure 17) show evidence for changes in outflow velocity with $W_{Ly\alpha}$ as well. Each Lyα profile exhibits a narrow peak redward of the systemic redshift (by construction, as they are stacked on the basis of their peak Lyα redshifts) as well as an extended blue wing, which broadens with decreasing $W_{Ly\alpha}$ (Figure 17). To quantify this effect, a two-component Gaussian fit was performed to each stacked Lyα profile with the following form:

$$f_\lambda(v) = A_{blue}\, e^{-(v+\Delta v/2)/2\sigma_{blue}} + A_{red}\, e^{-(v-\Delta v/2)/2\sigma_{red}} + f_{0,cont}\,, \quad (6)$$

such that the fit profile consists of two Gaussian peaks of arbitrary height and width, but with equal and opposite shifts with respect to systemic ($\pm\Delta v/2$). The model intentionally evokes an idealized outflow scenario in which the average LAE is surrounded by outflowing gas in both directions along the line of sight. In all three stacks, the red side of the Lyα profile diverges strongly from a Gaussian shape at large velocities, forming a broad red tail similar to that seen at $v \ll 0$. In order to maintain the simplicity of the model, the spectrum at $v > +500$ km s^{-1} was omitted from the fitting.

The resulting fits are displayed in Figure 17, with fit parameters given in Table 5. Both the width of the blue component and the separation of the blue and red peaks increases with decreasing $W_{Ly\alpha}$. While the Lyα peak width and separation may be increased by raising the H I column density, such a scenario would not predict a corresponding increase in the velocity width of metal absorption transitions, which have significantly smaller optical depths than Lyα. The similarity of the extended, blueshifted Lyα emission to the metal absorption profile therefore indicates that emission from outflowing gas likely populates the wings of the Lyα emission profile. That is, we suggest that the extended Lyα emission observed at large redshifts and blueshifts with respect to systemic depends sensitively on the outflow velocity, rather than merely the optical depth of the scattering medium. Models for this behavior, including the dependence of Lyα transmissivity on both the amplitude and velocity gradient of outflowing gas, are discussed in detail by Steidel et al. (2010, 2011).

Radiative transfer simulations of Lyα transmission suggest that these processes can generate double-peaked emission profiles with asymmetric offsets with respect to the systemic redshift. In particular, Verhamme et al. (2006) and others find that a spherical shell of gas expanding with velocity V_{exp} can in many cases produce a blue peak at $v = -V_{exp}$ and a red peak at $v = 2V_{exp}$. The stacked Lyα profiles in Figure 17 (or Figure 18, discussed below) are insensitive to the peak of the blue component and cannot discriminate between the two models (that is, whether the offset of the blue peak is equal to that of the red peak or half that of the red peak). However, the same qualitative relations hold for either model: the separation of the two peaks and the breadth of the extended blue and red components increases with increasing continuum luminosity.

4.3. Comparison to Continuum-bright Galaxies

While the trend of the inferred outflow properties with $W_{Ly\alpha}$ is weak among the LAEs in this sample, we can probe a much larger range in galaxy properties by extending the sample to include continuum-bright galaxies. In particular, the composite Lyα profile of the KBSS LBGs (Figure 18) displays a continuation of several trends identified among the LAE subsamples in Figure 17. The KBSS LBGs all have systemic redshift measurements, so we can compare the results of stacking them by either their nebular redshifts (Figure 18, left panel) or their Lyα-derived redshifts (right panel, as in Figure 17). While the detailed profile depends on which

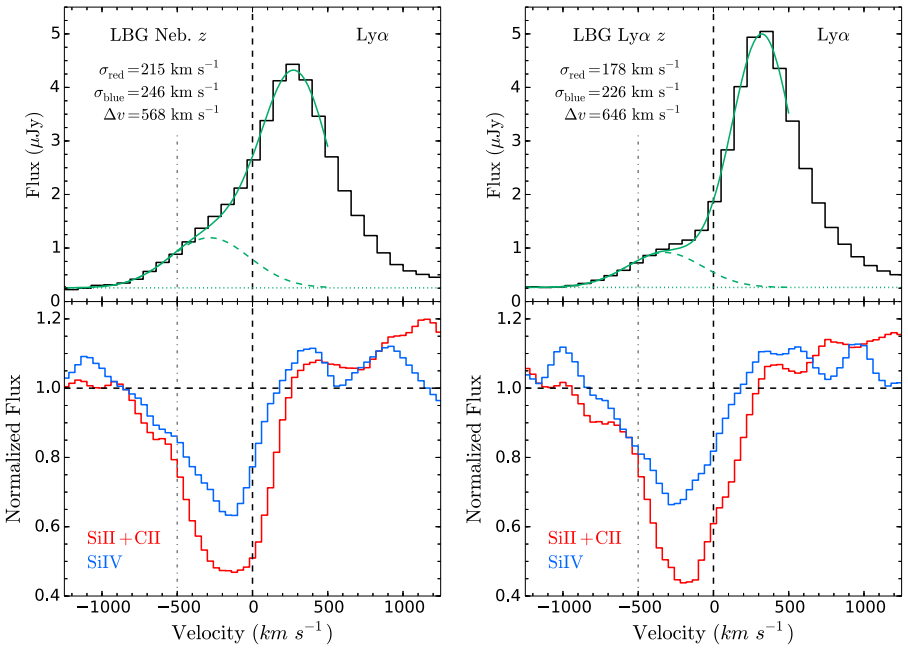

Figure 18. Composite Lyα emission and low/high-ionization absorption line profiles (as in Figure 17) for the KBSS LBG sample. Left: the composite spectrum is constructed using the nebular (systemic) redshift measurements. Right: the composite is constructed by stacking spectra according to their Lyα emission peak, in the same way as the LAE samples of Figure 17. As in Figure 7, the composite Lyα profile is distorted with respect to the composite constructed using systemic redshift measurements. However, the composite absorption profile is not significantly affected by the choice of nebular redshifts or calibrated Lyα redshifts.

redshift is employed, the LBG composites have broader and more widely separated peaks than any of the LAE subsamples, and the velocity extent of the broad tails of the Lyα emission again corresponds closely to the velocity extent of blueshifted absorption from the higher- and lower-ionization species. Note that the absorption profiles (bottom panels of Figure 18) are insensitive to which redshift indicator is used: the Si II λ1260, C II λ1334, and Si IV doublet absorption centroids each change by less than ∼25 km s^{-1} when stacked according to the nebular or calibrated Lyα redshifts. This consistency suggests that our measurements of interstellar absorption velocities in the LAE composite are unaffected by the scarcity of systemic redshifts among the LAE sample.

In Figures 19–21, we compare the stacked spectrum of all 318 LAEs in this sample with two stacks of LBGs: the KBSS LBG (Steidel et al. 2014) sample, and another sample from a survey for LyC emission in $z \sim 3$ galaxies (C. Steidel et al. 2015, in preparation). A comparison of these two samples to the KBSS-Lyα LAE sample is given in Table 6.

As discussed in Sections 2.2 and 3.2, the KBSS LBG sample consists of 65 galaxies that each exhibit Lyα emission in their UV spectra and have accurate systemic redshifts measured from rest-frame optical emission lines. These rest-UV spectra were observed using Keck/LRIS-B with the 600-line grism (the same used for the KBSS-Lyα LAEs), providing a spectral resolution $R \sim 1300$, or $\sigma_{inst} \approx 100$ km s^{-1}. There is significantly stronger metal absorption in each of the spectral lines shown in Figures 15 and 18, and the absorption profiles are both broader (extending to $v \approx -1000$ km s^{-1}) and deeper ($\lesssim$0.5× the continuum value) than the corresponding features in the LAE stack. The excited fine-structure and nebular emission lines (Figure 20), however, are well-matched to the

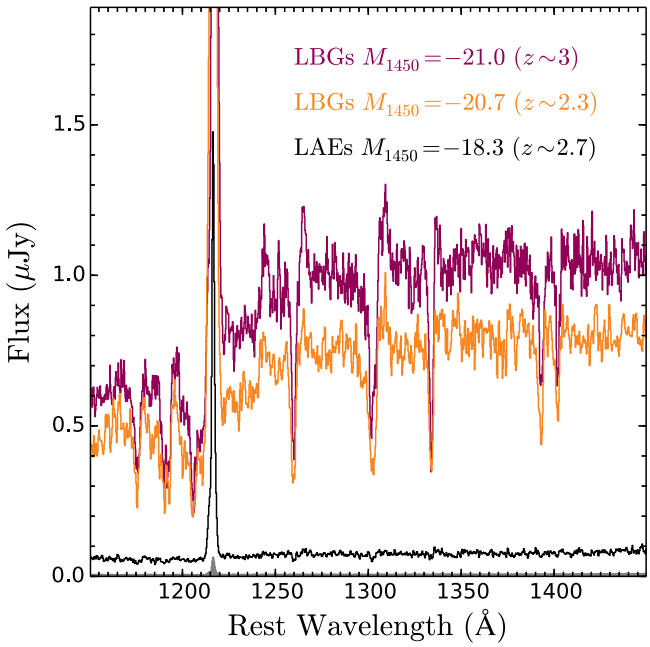

Figure 19. Composite UV continuum spectra for stacks of KBSS-Lyα LAEs and two comparison samples of LBGs. Details of the LBG samples are given in Table 6. The LAE stack (black, bottom) is the same as that in Figure 15, and the bootstrapped error spectrum is again shown in gray (primarily visible near the wavelength of the Lyα line). The KBSS LBG stack (orange, middle) has redshifts measured via nebular emission lines. The "LyC LBG" stack (purple, top) has redshifts measured by a calibrated combination of Lyα emission and metal absorption redshifts. All three composite spectra have $R \sim 1300$ for 1250 Å $< \lambda <$ 1400 Å. The challenge of measuring outflow signatures in faint LAEs is clear: not only is the continuum emission ∼10× fainter than typical LBGs, but the underlying absorption signatures are significantly weaker (Figure 20).

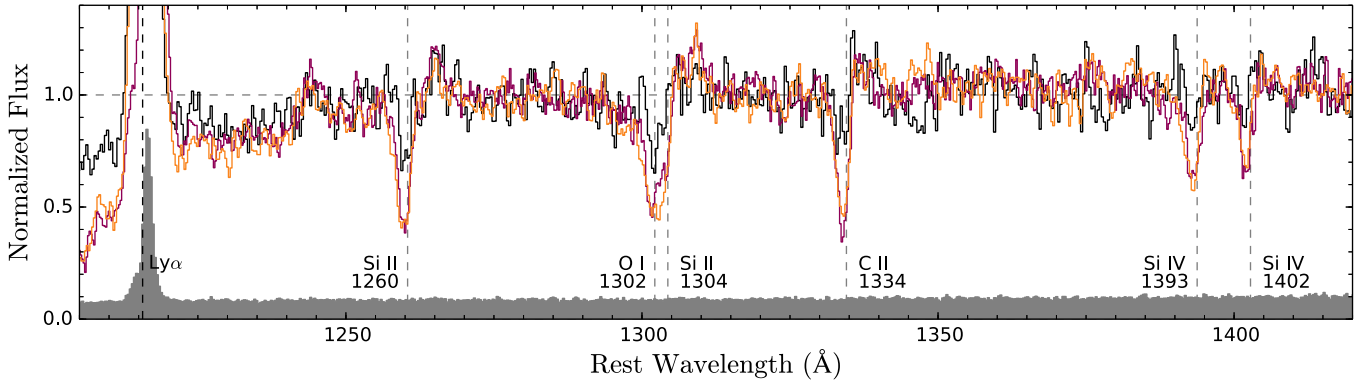

Figure 20. Composite rest-FUV continuum spectra (as in Figure 19) normalized to a common f_{1325} continuum level (1250 Å $< \lambda <$ 1400Å). As in the preceding figures, the bootstrapped LAE error spectrum is in gray. The absorption lines displayed in Figure 15 are here marked by vertical dashed lines. The two LBG samples (orange, purple) are highly consistent with each other and exhibit clear contrasts with the LAE sample, including significantly broader and deeper absorption profiles.

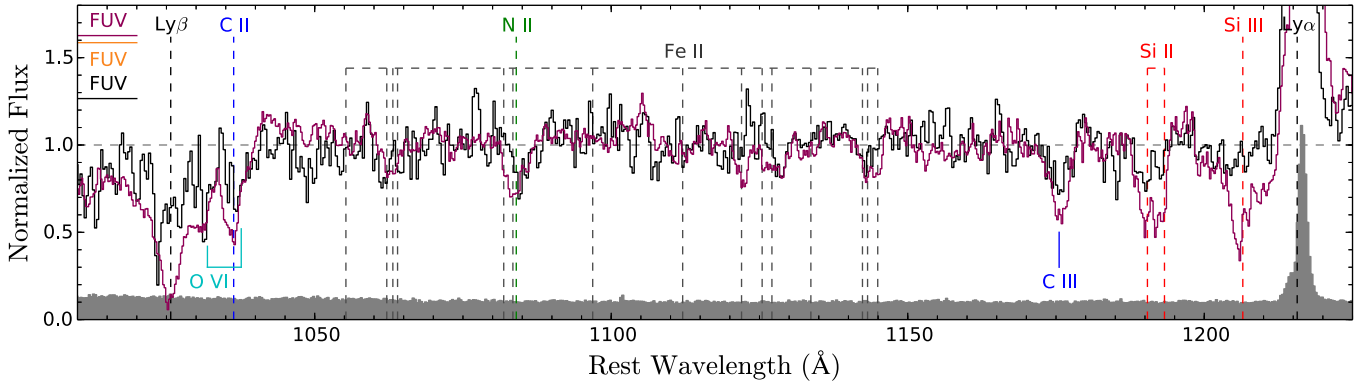

Figure 21. Composite rest-EUV continuum spectra (as in Figure 19) normalized to a common f_{1125} continuum level (1050 Å $< \lambda <$ 1200Å). Note that the normalizations differ from Figure 20: the continuum ratio f_{1325}/f_{1125} for each stack is shown here by the horizontal lines labeled "FUV" on the far left of the figure. The KBSS LBG composite is omitted due to the low S/N in this region, but the continuum ratio for that spectrum is marked with the orange horizontal line. As in the preceding figures, the bootstrapped LAE error spectrum is in gray. Insterstellar absorption lines are marked with vertical dashed lines, color-coded by atomic species and labeled from above. Horizontal dashed lines connect transitions of the same ion. Vertical solid lines labeled from below mark features with a photospheric component. Significant blending is visible due to both the absorption features and the many excited-state emission features throughout this region of the spectrum (not marked).

Table 6
Comparison of LAE and LBG Continuum and Absorption Properties

Sample	$\langle z \rangle$	m_{1450}[a] (mag)	M_{1450}[b] (mag)	$W_{Ly\alpha}$[c] (Å)	N_{obj}	$W_{Si\,II}$[d] (Å)	$v_{Si\,II}$[e] (km s^{-1})	$W_{C\,II}$[d] (Å)	$v_{C\,II}$[e] (km s^{-1})	$W_{Si\,IV}$[d] (Å)	$v_{Si\,IV}$[e] (km s^{-1})	f_c[f]
KBSS-Lyα	2.70	27.0	−18.3	42.7	318	0.53	−98	0.45	−185	0.51	−190	0.3
KBSS LBGs	2.36	24.4	−20.7	27.2	65	1.67	−224	1.35	−201	1.98	−276	0.6
LyC LBGs	3.07	24.6	−21.0	21.5	74	1.50	−172	1.44	−176	2.41	−288	0.6

Notes.
[a] m_{1450} is the observed AB magnitude corresponding to the rest-frame $\lambda \sim 1450$ Å UV continuum. At $z \sim 2.7$ (KBSS-Lyα and KBSS LBGs), this correponds to the G band, whereas the $\mathcal{R}$ magnitude is used for the LyC LBGs at $z \sim 3$. For consistency with the other samples, the LAE m_{1450} value is not Lyα-subtracted, though the Lyα emission dominates the broadband flux in many cases.
[b] M_{1450} is the absolute magnitude corresponding to m_{1450} at the typical redshift of the sample $\langle z \rangle$.
[c] Because the LBG samples have no narrowband Lyα images, all three values of $W_{Ly\alpha}$ here were measured spectroscopically for consistency. Note that the spectroscopic LAE sample has a mean photometric equivalent width $W_{Ly\alpha} = 85.6$ Å.
[d] $W_{Si\,II}$, $W_{C\,II}$, and $W_{Si\,IV}$ are the equivalent widths in absorption of Si II λ1260, C II λ1334, and Si IV λ1393+λ1402 (combined), respectively. See Table 4 and Figure 15.
[e] $v_{Si\,II}$, $v_{C\,II}$, and $v_{Si\,IV}$ are the absorption-weighted velocity of Si II λ1260, C II λ1334, and Si IV λ1393+λ1402.
[f] f_c is the covering fraction of low-ionization gas implied by the depth of the saturated Si II λ1260 absorption trough, which is consistent with the covering fraction implied by the depths of the O I λ1304 and C II λ1334 transitions in each composite spectrum.

corresponding LAE features, further validating the redshift offset employed for the KBSS-Lyα stack.

The LyC LBG sample consists of 74 galaxies, most of which do not have measured nebular redshifts; the redshifts for this sample were estimated via a combination of their Lyα emission and interstellar absorption redshifts with a calibration based on the results of Steidel et al. (2010) and Rakic et al. (2011). Furthermore, the composite spectrum was checked after

stacking using stellar photospheric features. About 15% of these galaxies have redshifts derived solely from the Lyα line and assume a 300 km s^{-1} offset (with respect to the Lyα centroid) based on stacks of the subset of objects with nebular emission redshifts. Like the LAE and KBSS LBG comparison samples, only objects with spectroscopically detected Lyα emission were included in the sample. The correspondence of the absorption and emission signatures of the stack to those of the KBSS LBG stack again demonstrates the efficacy of the calibration based on UV features. Being at higher redshifts than the other samples, these spectra were observed using a combination of the LRIS-R 600-line grating (covering the spectrum $\lambda_{\rm rest} \gtrsim 1200$ Å) and the LRIS-B 400-line grism (for $\lambda_{\rm rest} \lesssim 1200$ Å). This lower resolution was employed to maximize the S/N of the spectra shortward of Lyα (and the Lyman limit), where the observed spectrum becomes particularly faint. These spectra also have significantly larger integration times compared to the KBSS LBGs and KBSS-Lyα LAEs (8–10 versus 1.5–2 hr). Additionally, the higher redshifts of this sample ($z \sim 3$) with repect to the KBSS LBG sample ($z \sim 2.3$) cause the 1000 Å $< \lambda_{\rm rest} <$ 1200 Å continuum to lie at observed wavelengths with significantly higher LRIS-B throughput, further boosting the S/N of the LyC LBG composite spectrum at these wavelengths with respect to that of the KBSS LBGs. This stack is thus particularly useful for comparing the absorption due to Lyβ and other EUV transitions among the LBG and LAE samples (Figure 21).

The absorption profiles of the two LBG composite spectra are quite similar (Figure 20). The velocity extent of the absorption is almost identical in both samples ($v_{\rm max} \approx -1000$ km s^{-1}), though the LyC LBG stack shows slightly deeper absorption across all the lines. This difference may signify a difference in the galaxy properties: at $z \sim 3$, the LyC LBGs have a brighter average rest-UV luminosity than those at $z \sim 2.3$ (which have similar apparent magnitudes). The total equivalent width in interstellar absorption (Table 6), which is insensitive to the spectral resolution, is similar for the LyC and KBSS LBG stacks.

While the blending of Si II λ1304 with O I λ1302 inhibits a direct measurement of the Si II optical depth, Shapley et al. (2003) demonstrated that the Si II λ1260 transition is typically saturated in similar samples of bright LBGs, and the absorption of the Si II λ1190, λ1193, and λ1526 transitions in the LBG stacks are consistent with this interpretation. Furthermore, the consistency of the absorption profile depths among the low-ionization species in the LBG stacks suggests a gas covering fraction $f_c \sim 0.6$ for enriched, neutral/low-ionization material for the two LBG samples. The observed line ratio of the Si IV doublet is $W_{1393}/W_{1402} \sim 2$ for both LBG stacks (as in Shapley et al. 2003), suggesting optically thin absorption and $f_c \gtrsim 0.4$ for the ionized H II gas.

The difference in absorption line strength between the LBG and LAE samples can likewise be seen in the Lyβ transition (Figure 21). While the LBG composite is almost completely absorbed at the Lyβ line, the LAE spectrum has significantly higher transmission ($\gtrsim$50%). The continuum ratio f_{1325}/f_{1125} (displayed as horizontal lines on the left side of Figure 21) also varies significantly between the LBG and LAE samples: the LBG composites have a flux ratio $f_{1325}/f_{1125} \approx 1.6$, while the LAE composite has $f_{1325}/f_{1125} \approx 1.3$. The flux ratio for the $z \sim 3$ LyC LBG composite is uncertain because the spectra at $\lambda_{\rm rest} \gtrsim 1200$ Å and $\lambda_{\rm rest} \lesssim 1200$ Å fall on different detectors (LRIS-R and LRIS-B) within the spectrograph, so it is not entirely clear how much of the observed variation in continuum absorption is due to physical differences in the LAE and LBG galaxy populations, rather than the changing transmissivity of the IGM with redshift (e.g., Madau 1995). Both effects are likely to be present, as the UV continuum level blueward of Lyα is particularly sensitive to the dust content and metallicity of the ISM (the latter due to metal-line blanketing) and the age of the stellar population, all of which are observed to be lower among LAEs than LBGs.

Through comparison of the LAE and LBG stacks, it seems clear that the qualitative links between Lyα emission and and interstellar absorption discussed in Shapley et al. (2003) persist down to far fainter continuum luminosities than those probed by samples of LBGs. The outflow velocity (represented by either the absorption-weighted mean or the highest-velocity edge of absorption) decreases with increasing $W_{\rm Ly\alpha}$ across the LBG and LAE subsamples, and the covering fraction of gas drops steadily with increasing $W_{\rm Ly\alpha}$ to at least the intermediate subsample of LAEs ($W_{\rm Ly\alpha} \sim 37$ Å). The offset of the Lyα emission centroid likewise decreases from the LBG samples (+300 km s^{-1}) to the LAE stacks (+200 km s^{-1}). While further observations and modeling are required to determine the physics of star formation driven outflows, we suggest that our results provide an important link between the physical properties of these galaxies and those of the gas in and around them. We provide some initial interpretation of these results in the context of previous work below.

5. DISCUSSION

As described above, the UV continuum luminosities of these galaxies are closely linked to their SFRs, and our brighter samples of galaxies (e.g., LBGs and low-$W_{\rm Ly\alpha}$ LAEs) are associated with higher velocity dispersions and thus larger dynamical masses. Assuming that the SFR and stellar mass (M_*) are roughly proportional to the UV luminosity (i.e., the luminosity corresponding to M_{1450} in Table 6), the masses and SFRs of the KBSS LBGs likely exceed those of the LAEs by a typical factor ${\rm SFR}^{\rm LBG}/{\rm SFR}^{\rm LAE} \sim M_{*,\rm LBG}/M_{*,\rm LAE} \sim 10$. Similarly, the measured nebular velocity dispersions $\sigma_{\rm neb}$ are $\gtrsim 2\times$ larger for the LBG sample on average (Section 3.4; Figure 14), which likewise suggests $M_{\rm dyn,LBG}/M_{\rm dyn,LAE} \approx \sigma^2_{\rm LBG} a_{\rm LBG}/\sigma^2_{\rm LAE} a_{\rm LAE} \sim 10$, given the slightly larger physical sizes (a) of the typical KBSS LBGs (Erb et al. 2006b).

In comparison, various indicators of outflow velocity differ by a factor ~1.5–2 between the LAE and LBG samples: the Lyα emission centroid ($v_{\rm LAE} \approx 200$ km s^{-1}, $v_{\rm LBG} \approx 300$ km s^{-1}; Figures 17 and 18), the absorption centroid of low-ionization lines ($v_{\rm LAE} \approx -100$ km s^{-1}, $v_{\rm LBG} \approx -200$ km s^{-1};Table 6), and the maximum velocity of blueshifted absorption ($v_{\rm LAE} \approx 500$ km s^{-1}, $v_{\rm LBG} \approx 800$ km s^{-1}; Figures 17 and 18). This factor of ~1.5–2$\times$ in velocity over a 10$\times$ range in mass and SFR is broadly consistent with the scaling seen in samples of galaxies at at low and intermediate redshifts (Martin 2005; Rupke et al. 2005; Weiner et al. 2009), in which $v_{\rm outflow}$ is measured to scale as ${\rm SFR}^{0.2-0.35}$. This positive scaling stands in contrast to the lack of outflow velocity variation with either SFR or velocity dispersion observed by Steidel et al. (2010). In that paper, the authors note that their LBG samples have SFRs similar to the highest-SFR galaxies of Martin (2005) and Rupke et al. (2005),

where the relationship between SFR and $v_{\rm outflow}$ flattens off. Our LAEs are likely to have similar SFRs to the low-SFR galaxies of the low-redshift samples (SFR $\lesssim 10\,M_{\odot}\,{\rm yr}^{-1}$), so our results may indicate that the relationship between SFR and outflow velocity (i.e., positive scaling at low SFR, saturation at SFR $\gtrsim 10\,M_{\odot}\,{\rm yr}^{-1}$) is similar at low and high redshifts.

Analogously, the doubling of $\sigma_{\rm neb}$ between the LAE and LBG samples here suggests that outflow velocity grows in a roughly linear (or marginally sub-linear) fashion with the stellar dynamics of the galaxies. Similar scaling is observed in the lower-redshift samples noted above. Furthermore, if the escape speed scales as $v_{\rm esc} \approx 5-6\sigma_{\rm neb}$ (as discussed in Weiner et al. 2009), then the escape velocities of the LAEs are $v_{\rm esc} \approx 200$. This velocity is of order the typical absorption-weighted centroid velocity of the outflows (and significantly less than the maximum velocity of absorption), suggesting that a significant fraction of outflowing gas is permanantly ejected from the galaxy halos (similar to the lower-redshift results of Weiner et al. 2009). More detailed measurements of the masses and SFRs of individual LAEs are required to probe the scaling of these feedback processes within the sample of low-mass, high-redshift galaxies.

It may seem paradoxical that the centroid or width of the Lyα line is linked to outflow velocity and/or the SFR in a galaxy while the Lyα peak velocity at fixed resolution shows no dependence on continuum luminosity. In particular, Figures 17 and 18 seem to show a decoupling between the position of the narrow Lyα peak and the breadth of the extended Lyα emission tails to positive and negative velocities. We suggest that previous studies of Lyα emission actually show a similar decoupling between the Lyα peak and the width of the overall velocity distribution of Lyα flux. The radiative-transfer models employed by Kulas et al. (2012) and Chonis et al. (2013) seem to show that the dominant red peak of Lyα transmission through an expanding spherical shell of gas does not sensitively depend on gas velocity (at least for $v_{\rm gas} \lesssim 300\,{\rm km\,s}^{-1}$), but the distribution of flux in secondary and tertiary red and blue peaks becomes more extended with increasing gas velocity. These narrow emission line features are observed in higher-resolution spectra of bright and nearby galaxies (Verhamme et al. 2008; Chonis et al. 2013; Martin et al. 2015) and may be useful for modeling the effects of radiative transfer and gas velocity directly, but they are not feasibly observable in $L \sim 0.1L_{*}$ galaxies at $z \gtrsim 2$. We therefore suggest that the observed uniformity of the Lyα peak offset is due to the absorbing presence of *some* neutral gas at $v = 0$ in all of these star-forming galaxies (which sets the minimum velocity shift for an escaping Lyα photon), whereas the emission at larger (positive or negative) velocities reflects those photons scattered off of the high-velocity outflowing gas (which depends more strongly on galaxy properties). The broad wings of the Lyα emission line (e.g., Figure 17) are therefore likely to be populated by scattering off of outflowing gas, and thus are sensitive to the gas velocity and show a velocity distribution similar to that of the extended metal absorption.

However, the relatively low measured covering fractions of these outflows and the consistency of the Lyα peak offset may suggest that the majority of Lyα scatterings in LAEs occur without incurring any single large kinematic "kick" from an interaction with the highest-velocity gas. This tendency would be likely in a scenario where galaxy-scale outflows are highly anisotropic and thus create an orientation-dependent model for Lyα scattering and escape. The anisotropy of galaxy-scale outflows is highly favored by simulations (e.g., Hopkins et al. 2012) and lower-redshift observations (e.g., Kornei et al. 2012 at $z \sim 1$), both of which suggest that outflows dominate along the axis perpindicular to galactic disks, but it is not clear whether the anisotropy of the outflows and that of Lyα emissivity coincide. Verhamme et al. (2012) suggest that the Lyα flux and equivalent width are maximized when a galaxy is observed face-on. However this model would naively predict a positive correlation between Lyα velocity offset and equivalent width (rather than the anti- or absence of correlation observed) because both the Lyα emission and the line of sight outflow velocity would be maximized for face-on galaxy disks.

Local star-forming galaxies can help probe the geometry of Lyα escape. In particular, the LARS (Hayes et al. 2013; Östlin et al. 2014) consists of 14 local galaxies with *HST* imaging and spectroscopy of their Lyα emission. This sample was selected to provide a set of local analogs to high-redshift LAEs that can be observed at much higher spatial and spectral resolution. Rivera-Thorsen et al. (2015) use *HST*/COS spectra to analyze Lyα emission along with absorption due to Si II and Si IV along the line of sight to the brightest star-forming regions within these galaxies, finding several results broadly consistent with those of this paper. Rivera-Thorsen et al. use four spectrally resolved Si II transitions to show that the typical absorbing medium is optically thick, with a covering fraction that depends on both position and velocity. As in this paper, they find that higher local (and global) Lyα transmissivity is associated with low covering fractions of Si II, the Si II/Si IV absorption ratio is high at $v = 0$, and the resolved Lyα emission peak shows little dependence on outflow velocity.[16] The authors interpret these results in light of a model where Lyα escapes through an expanding medium that is both porous and non-uniform in velocity, with inhomogeneities potentially driven by Rayleigh–Taylor instabilities in expanding bubbles. Hayes et al. (2014) find that the Lyα emission is spatially extended with respect to the FUV continuum emission (in agreement with high-redshift studies); the local Lyα/Hα ratio is higher at larger galactocentric distances. In some edge-on disks, Lyα/Hα is seen to peak above and below the disk plane, but in most LARS galaxies the ratio appears to vary with no simple dependence on galaxy geometry or structure.

Furthermore, Law et al. (2009) find that most galaxies at $z \sim 2$–3 are not dynamically dominated by rotation and thus are less likely than low-redshift galaxies to generate coherent, collimated outflows. The young, faint populations of LAEs considered in this paper may be even less likely to maintain such structural coherence. Therefore, the KBSS-Lyα LAEs may be best modeled by irregular morphologies in which Lyα photons escape through a patchy ISM with minimal planar symmetry. Such a model, in which Lyα photons escape through "holes" in the neutral gas distribution, would similarly explain the possible association between Lyα and LyC emissivity (e.g., Mostardi et al. 2013).

[16] In contrast, Henry et al. (2015) argue that the covering fraction of neutral gas does not dominate Lyα escape in low-redshift, lower-mass galaxies, basing their claim on the appearance of Lyman-series absorption lines with zero residual transmission in COS spectra of Lyα-emitting Green Pea galaxies (GPs; Cardamone et al. 2009). However, the KBSS LAEs show significant transmission at Lyβ (Figure 21), suggesting that the gaseous environments of GPs are qualitatively different from those of $z \sim 2$–3 LAEs despite their similarly low masses and compact sizes.

LBGs and other bright star-forming galaxies can have extremely low Lyα and LyC escape fractions even when low-resolution spectroscopy suggests that the gas covering fractions are $f_c < 1$; in many cases, there may be extremely narrow, unresolved absorption components covering the line of sight that are still capable of absorbing all of the incident LyC flux (e.g., the galaxy Q0000-D6, as discussed by Shapley et al. 2003 and Giallongo et al. 2002). Opening up lines of sight through the neutral ISM that are transparent to both Lyα and LyC photons may be easier for low-mass galaxies.

Other mechanisms of Lyα escape could lead to decoupling between the Lyα and LyC emissivity of galaxies. While the scattering of Lyα photons is driven by H I, the eventual absorption and destruction of these photons is dominated by dust. If the LAEs contain little interstellar dust and have velocity fields capable of quickly scattering Lyα photons out of resonance, then a large fraction of Lyα photons may escape before encountering a dust particle (without requiring a "hole" in the H I distribution). If Lyα escape is dominated by this channel, then the Lyα and LyC escape fractions may be less strongly correlated, given that LyC photons are absorbed by H I rather than merely scattered. The apparent breakdown of the correlations of galaxy properties with $W_{\rm Ly\alpha}$ for the highest-$W_{\rm Ly\alpha}$ bin may indicate the transition to such a regime where dust formation and mixing into the ISM has not fully progressed. The faintest LAEs at $z \sim 2$–3 may be most analogous to those observed at $z \sim 6$, where the extremely blue UV slopes suggest that escaping photons encounter very little dust while exiting the galaxy. More robust fitting of the LAE spectral energy distributions, including deep NIR images from MOSFIRE, could strongly constrain the dust content of these young galaxies. Similarly, deep NIR spectra may constrain the metallicity (and thus the chemistry) of their ISM.

Another possibility is that the decoupling between Lyα emission and galaxy properties in this sample at the highest values of $W_{\rm Ly\alpha}$ may result from the contribution of the QSO ionizing radiation field to their Lyα flux. For fluorescently illuminated systems, the total Lyα flux is proportional to the surface area of optically thick H I and the strength of the local QSO-generated ionizing field (Cantalupo et al. 2005; Kollmeier et al. 2010), with minimal dependence on the kinematic or chemical properties of the galaxies. Our forthcoming analysis of the *HST* NIR and optical images of these fields will shed more light on the physical sizes, morphologies, and stellar components of the Lyα-emitting regions of these galaxies.

6. CONCLUSIONS

This paper has presented the rest-frame UV spectral properties of LAEs near HLQSOs at $z \sim 2.7$ from the KBSS-Lyα survey. These LAEs are significantly fainter ($L \sim 0.1L_*$) than previous spectroscopic samples of high-redshift star-forming galaxies, which enables us to extend observations of interstellar enrichment and kinematics to a new galaxy regime. Our primary results are as follows.

1. The faint LAEs have Lyα escape fractions $f_{\rm esc,Ly\alpha} \approx 30\%$ (based on the observed Lyα to Hα flux ratio), significantly higher than previous observations of brighter star-forming galaxies at high-redshift (Section 3.1). This result is consistent with the conclusions of Steidel et al. (2011).
2. Like continuum-bright galaxies at similar redshifts, LAEs produce Lyα emission that is significantly shifted from the systemic redshift. While the flux-weighted Lyα emission centroid varies with galaxy luminosity across our combined sample of LAEs and LBGs, the Lyα peak (when observed with $R \approx 1300$) displays a highly consistent shift of $\sim$200 km s^{-1} irrespective of continuum luminosity. This offset may be used to estimate redshifts of diverse Lyα-emitting galaxies observed at comparable resolution when rest-frame optical spectroscopy is unavailable (Section 3.2).
3. Faint LAEs display a range of diverse Lyα morphologies and are associated with narrower Lyα peaks with smaller peak separations than those of LBGs. These results are consistent with smaller velocities and/or column densities of neutral gas in the CGM of LAEs compared to LBGs. While most of the Lyα emission lines have a characteristic red-dominant morphology, there is a minority (13%, 4 objects) with blueshifted primary peaks (Sections 3.2–3.4).
4. By combining the UV continuum spectra of all 318 LAEs in our spectroscopic sample, we find absorption signatures of several metal ions that have been shown to trace outflowing material in more luminous star-forming galaxies. We believe these are the first measurements of metal-enriched outflowing gas in such faint high-redshift galaxies. We measure absorption-weighted velocities of $\sim$100–200 km s^{-1} and maximum velocities of $\sim$500 km s^{-1}, both significantly smaller than those seen in comparison samples of LBGs (Section 4).
5. Using multiple transitions of Si II, we infer the saturation of the Si II λ1260 transition, thereby constraining the covering fraction of low-ionization material in front of the LAEs to $f_c \approx 0.3$. This covering fraction is significantly smaller than that observed in LBGs, with $f_c \sim 0.5$–0.7 in the same ions. This low covering fraction of obscuring gas likely drives the observed high escape fractions of Lyα and Ly-continuum photons from faint galaxies (Section 4.1).
6. We find that outflow velocity—whether probed by maximum velocity of metal absorption, absorption-weighted mean velocity, or Lyα emission morphology—increases with continuum luminosity (decreases with Lyα equivalent width) among LAEs and with respect to LBGs. This result suggests that these gas outflows are tied to physical properties of their associated galaxies—e.g., the mass and SFR, for which the nebular velocity dispersion and continuum luminosity are proxies. In particular, our results are consistent with weak dependence of outflow velocity on SFR ($v_{\rm outflow} \sim {\rm SFR}^{0.25}$), and we find that the outflow velocities (up to 500 km s^{-1}) are large compared to the probable $\sim$200 km s^{-1} escape velocities of the LAEs (Section 5).

In sum, these observations demonstrate that stellar feedback is an essential ingredient in realistic simulations of even the youngest, least massive galaxies at high redshift. In particular, these feedback processes are key to understanding the escape of line and continuum photons (particularly ionizing photons) from faint galaxies and their effect on their surrounding IGM. Further work is necessary to analyze the apparent absence of correlations between $W_{\rm Ly\alpha}$ and covering fraction of ISM absorption at the highest equivalent widths. This effect may be the result of a qualitative transition in the properties of galaxies to those with minimal enrichment and dust, and could

also point to the effect of the QSO in picking out galaxies independently of their SFRs.

In each of these topics, further progress will be driven by continued near-IR observations of faint galaxy populations. Rest-frame optical spectra (in combination with observations in the rest-UV) are the only way to effectively constrain the SFRs, metal enrichment, and gas kinematics of these newborn galaxies, thereby establishing the relationships between their stellar and gaseous properties and characterizing evolution of the baryon cycle over cosmic time.

We are indebted to the staff of the W.M. Keck Observatory who keep the instruments and telescopes running effectively. We also wish to extend thanks to those of Hawaiian ancestry on whose sacred mountain we are privileged to be guests. This work has been supported in part by the US National Science Foundation through grants AST-0908805 and AST-1313472. We thank Mariska Kriek and Eliot Quataert for many useful discussions as well as the anonymous referee for comments and suggestions that significantly improved this work. R.F.T. also acknowledges support from Dennis and Carol Troesh and from the Miller Institute for Basic Research in Science at the University of California, Berkeley.

REFERENCES

Adelberger, K. L., Shapley, A. E., Steidel, C. C., et al. 2005, ApJ, 629, 636
Adelberger, K. L., Steidel, C. C., Kollmeier, J. A., & Reddy, N. A. 2006, ApJ, 637, 74
Adelberger, K. L., Steidel, C. C., Shapley, A. E., & Pettini, M. 2003, ApJ, 584, 45
Aguirre, A., Hernquist, L., Schaye, J., et al. 2001, ApJ, 561, 521
Ando, M., Ohta, K., Iwata, I., et al. 2006, ApJL, 645, L9
Andrews, B. H., & Martini, P. 2013, ApJ, 765, 140
Atek, H., Kunth, D., Schaerer, D., et al. 2014, A&A, 561, A89
Birnboim, Y., & Dekel, A. 2003, MNRAS, 345, 349
Brocklehurst, M. 1971, MNRAS, 153, 471
Cantalupo, S., Lilly, S. J., & Haehnelt, M. G. 2012, MNRAS, 425, 1992
Cantalupo, S., Lilly, S. J., & Porciani, C. 2007, ApJ, 657, 135
Cantalupo, S., Porciani, C., Lilly, S. J., & Miniati, F. 2005, ApJ, 628, 61
Cardamone, C., Schawinski, K., Sarzi, M., et al. 2009, MNRAS, 399, 1191
Chonis, T. S., Blanc, G. A., Hill, G. J., et al. 2013, ApJ, 775, 99
Ciardullo, R., Gronwall, C., Adams, J. J., et al. 2013, ApJ, 769, 83
Ciardullo, R., Zeimann, G. R., Gronwall, C., et al. 2014, ApJ, 796, 64
Dijkstra, M., Haiman, Z., & Spaans, M. 2006, ApJ, 649, 14
Dopita, M. A., & Sutherland, R. S. 2003, Astrophysics of the Diffuse Universe (Berlin, New York: Springer), 2003
Dressler, A., Henry, A., Martin, C. L., et al. 2015, ApJ, 806, 19
Erb, D. K., Shapley, A. E., Pettini, M., et al. 2006a, ApJ, 644, 813
Erb, D. K., Steidel, C. C., Shapley, A. E., et al. 2006b, ApJ, 646, 107
Erb, D. K., Steidel, C. C., Trainor, R. F., et al. 2014, ApJ, 795, 33
Gawiser, E., van Dokkum, P. G., Gronwall, C., et al. 2006, ApJL, 642, L13
Giallongo, E., Cristiani, S., D'Odorico, S., & Fontana, A. 2002, ApJL, 568, L9
Giavalisco, M., Koratkar, A., & Calzetti, D. 1996, ApJ, 466, 831
Hashimoto, T., Ouchi, M., Shimasaku, K., et al. 2013, ApJ, 765, 70
Hayes, M., Östlin, G., Duval, F., et al. 2014, ApJ, 782, 6
Hayes, M., Östlin, G., Schaerer, D., et al. 2010, Natur, 464, 562
Hayes, M., Östlin, G., Schaerer, D., et al. 2013, ApJL, 765, L27
Henry, A., Scarlata, C., Martin, C. L., & Erb, D. 2015, arXiv:1505.05149
Hogan, C. J., & Weymann, R. J. 1987, MNRAS, 225, 1P
Hogg, D. W., Cohen, J. G., Blandford, R., & Pahre, M. A. 1998, ApJ, 504, 622
Hopkins, P. F., Kereš, D., Oñorbe, J., et al. 2014, MNRAS, 445, 581
Hopkins, P. F., Quataert, E., & Murray, N. 2012, MNRAS, 421, 3522
Hummels, C. B., Bryan, G. L., Smith, B. D., & Turk, M. J. 2013, MNRAS, 430, 1548
Jones, T., Stark, D. P., & Ellis, R. S. 2012, ApJ, 751, 51
Jones, T. A., Ellis, R. S., Schenker, M. A., & Stark, D. P. 2013, ApJ, 779, 52
Kennicutt, R. C., Jr. 1998, ARA&A, 36, 189
Kereš, D., Katz, N., Davé, R., Fardal, M., & Weinberg, D. H. 2009, MNRAS, 396, 2332
Kereš, D., Katz, N., Weinberg, D. H., & Davé, R. 2005, MNRAS, 363, 2
Kollmeier, J. A., Zheng, Z., Davé, R., et al. 2010, ApJ, 708, 1048
Kornei, K. A., Shapley, A. E., Erb, D. K., et al. 2010, ApJ, 711, 693
Kornei, K. A., Shapley, A. E., Martin, C. L., et al. 2012, ApJ, 758, 135
Kulas, K. R., Shapley, A. E., Kollmeier, J. A., et al. 2012, ApJ, 745, 33
Kunth, D., Mas-Hesse, J. M., Terlevich, E., et al. 1998, A&A, 334, 11
Law, D. R., Steidel, C. C., Erb, D. K., et al. 2009, ApJ, 697, 2057
Madau, P. 1995, ApJ, 441, 18
Martin, C. L. 2005, ApJ, 621, 227
Martin, C. L., Dijkstra, M., Henry, A., et al. 2015, ApJ, 803, 6
Martin, C. L., Scannapieco, E., Ellison, S. L., et al. 2010, ApJ, 721, 174
Martin, C. L., Shapley, A. E., Coil, A. L., et al. 2012, ApJ, 760, 127
Mas-Hesse, J. M., Kunth, D., Tenorio-Tagle, G., et al. 2003, ApJ, 598, 858
Matsuda, Y., Yamada, T., Hayashino, T., et al. 2004, AJ, 128, 569
McLean, I. S., Steidel, C. C., Epps, H., et al. 2010, Proc. SPIE, 7735, 77351E
McLean, I. S., Steidel, C. C., Epps, H. W., et al. 2012, Proc. SPIE, 8446, 84460J
McLinden, E. M., Finkelstein, S. L., Rhoads, J. E., et al. 2011, ApJ, 730, 136
Mostardi, R. E., Shapley, A. E., Nestor, D. B., et al. 2013, ApJ, 779, 65
Nestor, D. B., Shapley, A. E., Kornei, K. A., Steidel, C. C., & Siana, B. 2013, ApJ, 765, 47
Östlin, G., Hayes, M., Duval, F., et al. 2014, ApJ, 797, 11
Ouchi, M., Shimasaku, K., Akiyama, M., et al. 2008, ApJS, 176, 301
Partridge, R. B., & Peebles, P. J. E. 1967, ApJ, 147, 868
Pettini, M., Madau, P., Bolte, M., et al. 2003, ApJ, 594, 695
Pettini, M., Rix, S. A., Steidel, C. C., et al. 2002, ApJ, 569, 742
Pettini, M., Shapley, A. E., Steidel, C. C., et al. 2001, ApJ, 554, 981
Pettini, M., Steidel, C. C., Adelberger, K. L., Dickinson, M., & Giavalisco, M. 2000, ApJ, 528, 96
Rakic, O., Schaye, J., Steidel, C. C., & Rudie, G. C. 2011, MNRAS, 414, 3265
Reddy, N. A., Steidel, C. C., Pettini, M., et al. 2008, ApJS, 175, 48
Rivera-Thorsen, T. E., Hayes, M., Östlin, G., et al. 2015, ApJ, 805, 14
Robertson, B. E., Furlanetto, S. R., Schneider, E., et al. 2013, ApJ, 768, 71
Rudie, G. C., Steidel, C. C., Shapley, A. E., & Pettini, M. 2013, ApJ, 769, 146
Rudie, G. C., Steidel, C. C., Trainor, R. F., et al. 2012, ApJ, 750, 67
Rupke, D. S., Veilleux, S., & Sanders, D. B. 2005, ApJS, 160, 115
Schenker, M. A., Ellis, R. S., Konidaris, N. P., & Stark, D. P. 2013, ApJ, 777, 67
Shapley, A. E., Steidel, C. C., Pettini, M., & Adelberger, K. L. 2003, ApJ, 588, 65
Shibuya, T., Ouchi, M., Nakajima, K., et al. 2014, ApJ, 788, 74
Stark, D. P., Ellis, R. S., Chiu, K., Ouchi, M., & Bunker, A. 2010, MNRAS, 408, 1628
Steidel, C. C., Adelberger, K. L., Shapley, A. E., et al. 2003, ApJ, 592, 728
Steidel, C. C., Bogosavljević, M., Shapley, A. E., et al. 2011, ApJ, 736, 160
Steidel, C. C., Erb, D. K., Shapley, A. E., et al. 2010, ApJ, 717, 289
Steidel, C. C., Giavalisco, M., Pettini, M., Dickinson, M., & Adelberger, K. L. 1996, ApJL, 462, L17
Steidel, C. C., Rudie, G. C., Strom, A. L., et al. 2014, ApJ, 795, 165
Steidel, C. C., Shapley, A. E., Pettini, M., et al. 2004, ApJ, 604, 534
Trainor, R., & Steidel, C. C. 2013, ApJL, 775, L3
Trainor, R. F., & Steidel, C. C. 2012, ApJ, 752, 39
Turner, M. L., Schaye, J., Steidel, C. C., Rudie, G. C., & Strom, A. L. 2014, MNRAS, 445, 794
Verhamme, A., Dubois, Y., Blaizot, J., et al. 2012, A&A, 546, A111
Verhamme, A., Schaerer, D., Atek, H., & Tapken, C. 2008, A&A, 491, 89
Verhamme, A., Schaerer, D., & Maselli, A. 2006, A&A, 460, 397
Weiner, B. J., Coil, A. L., Prochaska, J. X., et al. 2009, ApJ, 692, 187
White, S. D. M., & Frenk, C. S. 1991, ApJ, 379, 52
Wofford, A., Leitherer, C., & Salzer, J. 2013, ApJ, 765, 118
Yamada, T., Matsuda, Y., Kousai, K., et al. 2012a, ApJ, 751, 29
Yamada, T., Nakamura, Y., Matsuda, Y., et al. 2012b, AJ, 143, 79
Zheng, Z., & Miralda-Escudé, J. 2002, ApJ, 578, 33
Zheng, Z., & Wallace, J. 2014, ApJ, 794, 116